Electrical resistivity structure of the upper mantle beneath Northeastern China: Implications for rheology and the mechanism of craton destruction

Zeyi Dong [a], Ji Tang [a], Martyn Unsworth [b,*], Xiaobin Chen [a]

[a] *Institute of Geology, China Earthquake Administration, Beijing 100029, China*
[b] *Department of Physics, University of Alberta, Edmonton T6G 2J1, Canada*

ARTICLE INFO

ABSTRACT

The North China Craton (NCC) and Central Asian Orogen Belt (CAOB) in Northeastern China experienced a range of tectonic events during the Phanerozoic, dominated by lithospheric thinning of the eastern NCC in the late Mesozoic and Cenozoic. In order to better understand the tectonic evolution of the NCC and the CAOB, new broadband and long period magnetotelluric data were collected along a north-west to southeast trending profile that extended from the CAOB across the Yanshan Belt, the Tanlu Fault Zone to the Liaodong Peninsula. A two-dimensional (2-D) resistivity model was derived from inversion of the transverse electric mode, transverse magnetic mode and vertical magnetic field data.

In the crust of the CAOB, the resistivity model shows a northwest dipping low resistivity zone beneath the Solonker suture that is identified as the suture zone formed by the collision between the Siberian and North China cratons.

The upper mantle of the CAOB is characterized by moderate resistivity values (300–1000 Ω m) that are best explained by the presence of hydrogen dissolved in olivine. The water concentration of the CAOB mantle is comparable to values reported for the asthenosphere and cratons that have been significantly hydrated. The NCC upper mantle is generally lower in resistivity than the CAOB upper mantle, and a zone of lower resistivity is observed in the upper mantle at the southeast end of the profile beneath the NCC (<100 Ω m) which requires around 1% partial melt to account for the observed resistivity.

Superimposed on this southeast decrease in upper mantle resistivity, three low resistivity zones were imaged: (1) below the Xilamulun fault, (2) close to the North–South Gravity Lineament, and (3) between the northern Yanshan Belt and Tanlu Fault Zone. The low resistivities can be explained as regions of partial melts or fluids, perhaps caused by asthenospheric upwelling.

Together with seismic imaging results and geochemical data, the resistivity model shows that the modification of the lithosphere associated with craton destruction has occurred in a spatially non-uniform manner in the region of the NCC investigated in this study.

1. Introduction

Cratons are lithospheric blocks that have remained stable for billions of years, and their longevity has often been attributed to their buoyancy and rigidity. Recent research suggests that these factors may not be sufficient to prevent cratons being destroyed by mantle convection (O'Neill et al., 2008). It has been suggested that it is the low water content of cratonic lithosphere which causes the high strength and allows cratons to survive for billions of years (Peslier et al., 2010). Under certain circumstances, the cra-

tonic lithosphere can be weakened and the craton destroyed. A key part of this process may be the hydration of the cratonic lithospheric upper mantle, which will lower the strength. This type of hydration is occurring today in the Southwest United States, where water was transported into the upper mantle by the subducted Farallon Plate (Li et al., 2008).

Another location where this process may be at work is beneath the eastern North China Craton (NCC). The westward subduction of the Pacific Plate resulted in the NCC being located within the back arc region of the subduction zone. Elevated back arc temperatures led to extensive magmatism and deformation (Niu, 2005; Wu et al., 2003, 2005; Xu et al., 2009; Zhang, 2009). Since the water content controls the strength of the lithospheric upper mantle, a study of

* Corresponding author. Tel.: +1 (780) 492 3041.
E-mail address: unsworth@ualberta.ca (M. Unsworth).

craton destruction should use geophysical methods that can determine the water content of the mantle. Magnetotellurics is one such method and is used in this paper.

The lithosphere of the Northeastern NCC had a complex history prior to the onset of craton destruction. During the Late Permian to Early Triassic, the NCC was sutured to the Central Asian Orogenic Belt (CAOB) in the north along the Solonker suture zone (Xiao et al., 2003) (Fig. 1). After the collision, a phase of post-collisional extension took place and formed the Xilamulun tectonic–metallogenic belt (Zhang et al., 2009). Subduction of the Pacific Plate beneath Northeast China began in the Late Mesozoic and continues to the present (Kusky et al., 2007). Craton destruction began in the Mesozoic and continued into the Cenozoic, as the eastern NCC experienced significant thermo-tectonic reactivation which led to widespread lithospheric extension and magmatic activity (Windley et al., 2007). This reactivation process resulted in the lower part of the 200 km thick lithosphere being heated, removed and partially replaced by hot material to give a lithosphere that is only 60–80 km thick. It also changed the physical–chemical properties of the lithospheric mantle, as indicated by geochemical and petrological studies (Menzies et al., 1993; Griffin et al., 1998; Xu, 2001; Wu et al., 2006; Zheng et al., 2007a; Zhang et al., 2008). Deformation continues today, as evidenced by frequent intraplate earthquakes (China Earthquake Networks Center, 2013).

In recent years, seismic studies have been used to image the lithosphere of the NCC and investigate the present day structure (Chen et al., 2006, 2008, 2009, 2010; Chen, 2009, 2010; Zhang et al., 2007; Zheng et al., 2008, 2012; Tang and Chen, 2008; Huang et al., 2009; Li and Niu, 2010; Zhao et al., 2010; Xu et al., 2011; Wei et al., 2011; Li and He, 2011). Magnetotelluric (MT) data provide constraints on lithospheric composition that can complement those obtained from seismic studies, especially with regard to the presence of volatile phases (Hirth et al., 2000). This is important because even small amounts of water and partial melt can have profound impacts on the rheology of the crust and upper mantle. This paper describes a 1200 km NW–SE MT profile in NE China (Fig. 1) which includes the first long period magnetotelluric measurements made on the Northeastern NCC. The profile was collected to address some of the outstanding tectonic questions regarding the lithospheric structure and history of Northeast China including:

(1) What is the present day fluid distribution and rheology of the lithosphere beneath the CAOB and NCC? Resistivity models derived from MT data provide valuable constraints on the water content of the upper mantle (Selway, 2014) which in turn have a major influence on lithospheric strength.
(2) What does the present day structure imply about the mechanism by which lithospheric removal occurred during craton destruction?

2. Geological and geophysical background

2.1. Geological setting

Northeastern China consists of two major tectonic elements, the Central Asian Orogenic Belt (CAOB) in the north, and the North China Craton (NCC) in the south (Fig. 1).

The CAOB is approximately 300 km wide and located between the NCC and the Siberian Craton (Fig. 1). It is comprised of a number of Neoproterozoic–Phanerozoic accretionary complexes, and extends from the Altai Mountains in the west to eastern Siberia (Xiao et al., 2003). It was formed by north–south-directed subduction of the Paleo-Asian Ocean during the Paleozoic, which ultimately led to the suturing of the NCC to the southern edge of the

CAOB. Most researchers favor a date in the late Permian to early Triassic for the terminal collision along the Solonker suture zone (Xiao et al., 2003; Miao et al., 2007; Windley et al., 2007). The Xilamulun Fault and Chifeng-Kaiyuan Fault are major litho-tectonic boundaries also formed during the closure of the Paleo-Asian Ocean (Zeng et al., 2011).

The North China Craton (NCC) is the oldest continental fragment in China. The Archean to Paleoproterozoic basement rocks are overlain by Mesoproterozoic to Cenozoic sedimentary cover (Liu et al., 1992; Zhao et al., 2003). The NCC is composed of two Archean continental blocks: the Eastern and Western blocks which have experienced very different geological histories, and are separated by the Paleoproterozoic Trans-North China Orogen (Zhao et al., 2001, 2005) (Fig. 1b). The Western Block has been stable since the early Proterozoic (1.85 Ga) with minor deformation since the end of the Paleozoic. In contrast, the Eastern Block has undergone significant tectonic changes during the Phanerozoic as described below. Since the Triassic, tectonic events have been focused in the Eastern Block of the NCC and have been dominated by the Mesozoic–Cenozoic craton destruction. This has resulted in a thinned lithospheric mantle, an increase in heat flow, widespread volcanism and formation of large-scale sedimentary basins (Griffin et al., 1998; Fan et al., 2000; Zhou et al., 2002). It has generated two major geological and geophysical lineaments:

(1) The NNE striking North–South Gravity Lineament (NSGL) is a remarkable feature, that is 100 km wide and extends over 3500 km in a N–S direction across most of eastern China and traverses the NCC (Fig. 1). Within the NCC, the NSGL separates areas to the west that have negative Bouguer anomalies, low heat flow, high mantle seismic velocities, thicker lithosphere and mountainous topography, from low-lying areas to the east that have zero to slightly positive gravity anomalies, high heat flow, lower mantle seismic velocities, thinner lithosphere (Xu, 2007; Windley et al., 2007).
(2) The Tanlu Fault Zone (TLFZ) is a major strike-slip fault zone that bisects the eastern NCC. It is up to 500 km wide and extends from the Yangtze River to the Russian Far East. The TLFZ has accumulated over 700 km of left-lateral offset, mostly during the Cretaceous (Xu et al., 1987; Xu and Zhu, 1994). Motion on the TLFZ may be related to asthenospheric upwelling and lithospheric reactivation of the eastern NCC since the Mesozoic (Zheng et al., 1998; Xu et al., 2004; Chen et al., 2006). Over 1000 earthquakes with magnitude Ms > 2.0 have occurred on the northern TLFZ since the 1950s (Fig. 2). The largest recent earthquake was the left lateral Ms = 7.3 1975 Haicheng earthquake (China Earthquake Networks, 2013; Cipar, 1979).

2.2. Previous geophysical studies

The North China Interior Structure Project (NCISP) collected a number of broadband seismic profiles in the NCC and adjacent areas (Chen et al., 2010). Zheng et al. (2007b) used teleseismic receiver functions to develop a crustal S-wave velocity model for the northern margin of the NCC (NCISP III in Fig. 3a) which showed that the crust beneath the Yanshan Belt was 30–40 km thick, with significant lateral variations and a sharply defined Moho. Shear wave splitting gave evidence for a complex pattern of upper mantle deformation beneath the YSB and CAOB (Zhao and Zheng, 2007) and suggested that lithospheric thinning had occurred primarily by delamination along the northern edge of the NCC. Chen et al. (2008) studied the northeastern NCC with S-wave receiver function migration and detected strong lateral variations in lithospheric thickness. They reported that the lithosphere beneath the
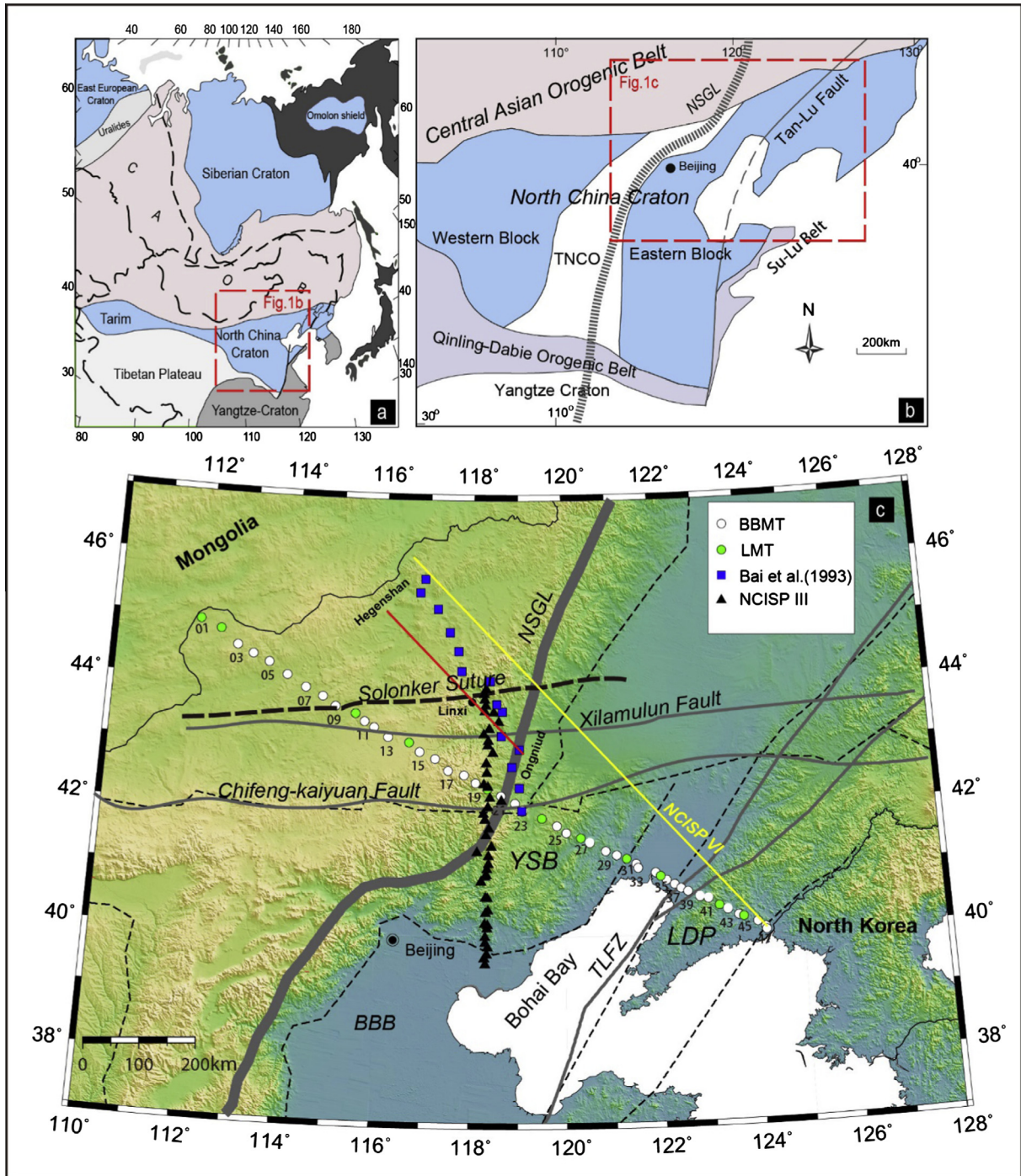
Fig. 1. (a) Sketch map of east Asia and adjacent areas (modified from Kröner et al., 2008). (b) A simplified tectonic mp division of the North China Craton (after Yang et al., 2012). NSGL: North–South Gradient Lineament. (c) Topography of Northeastern China with MT stations (circles). Black triangles are seismic stations from the NCISP-III (Zheng et al., 2007b). Blue squares show previous MT stations in this region (Bai et al., 1993a,b). The yellow line represents the NICISP VI line (www.seislab.cn) (Wei et al., 2011). The thin dashed lines represent tectonic boundaries. The cross section from Hegenshan to Ongniud (Lu and Xia, 1993) is marked by the red line. The gray lines show the main faults in the study region. BBB = Baihai Basin; CAOB = Central Asian Orogen Belt; LDP = Liaodong Peninsula; NCC = North China Craton; TLFZ = Tanlu Fault Zone; TNCO = Trans North China Orogen; YC = Yangtze Craton; YSB = Yanshan Belt. (For interpretation of the references to color in this figure legend, the reader is referred to the web version of this article.)

northern Yanshan Belt was 100–130 km thick and thinned to just 60–70 km beneath the TLFZ. Tang and Chen (2008) used surface wave data on profile NCISP III (Fig. 3d) to image undulations in the lithosphere–asthenosphere boundary. They speculated these may have resulted from uneven lithospheric thinning, and that the thick lithospheric lid in the northern Yanshan Belt may have separated mantle convection into separate domains on and off

the craton. Wei et al. (2011) estimated the crustal thickness and average crustal V_p/V_s ratio along NCISP VI from receiver functions. Li and He (2011) imaged the lithospheric structure of the NCISP VI (Fig. 3b) using Rayleigh wave dispersion inversion and reported a sharp change in lithospheric thickness close to the NSGL. Zhao et al. (2012) present new high resolution tomographic images which show that significant heterogeneity extends to depths
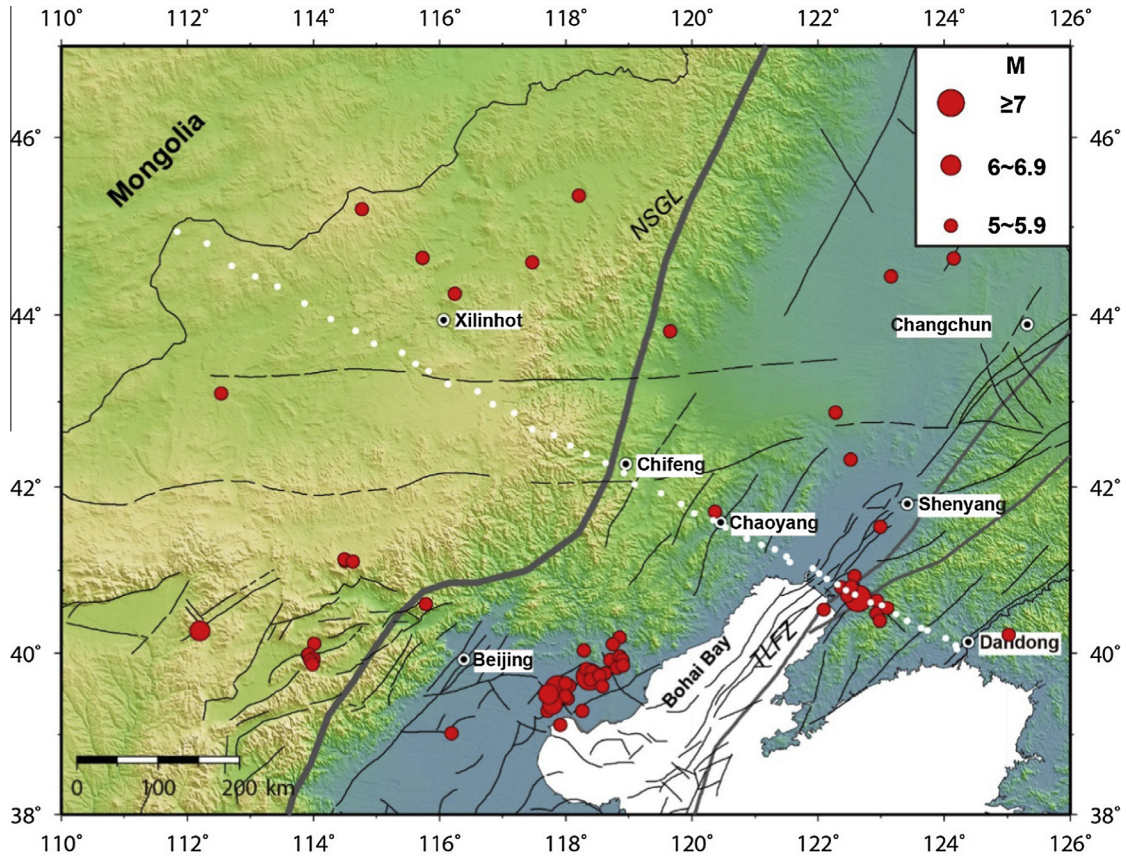
Fig. 2. Seismicity with magnitudes greater than *M* = 5.0 in the study area from 1950 to 2013 (China Earthquake Networks, Seismic Data Management and Service System, http://www.csndmc.ac.cn/newweb/index.jsp). The thin black lines are active faults and the white dots correspond to MT stations.
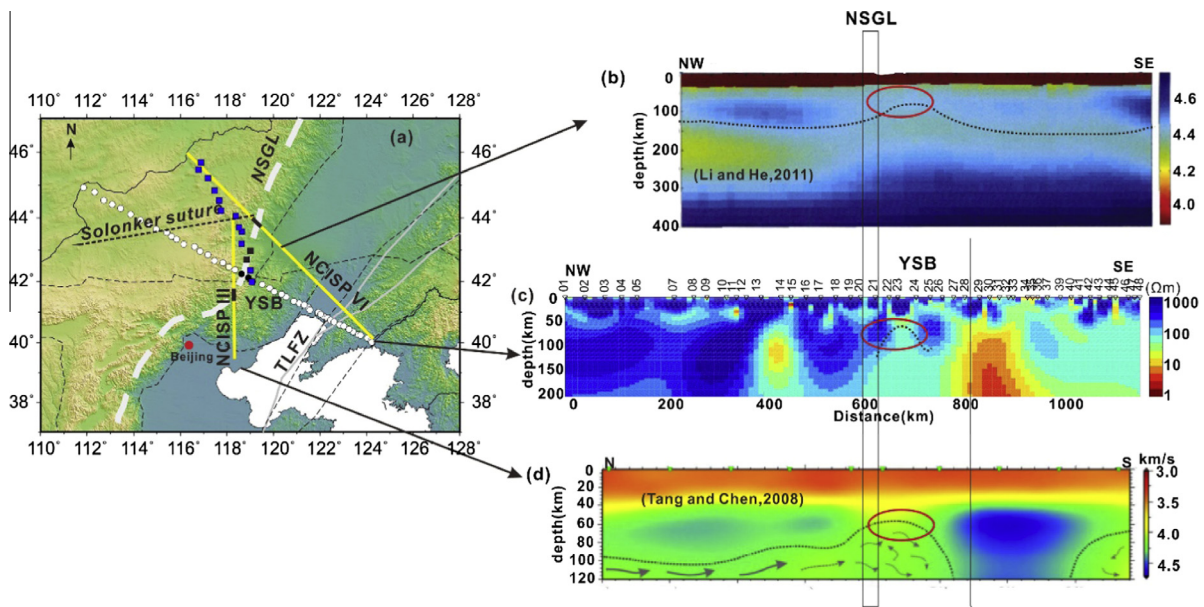

Fig. 3. (a) Yellow lines represent the NCISP-VI and NCISP-III profiles of the Seismic Array Laboratory, Institute of Geology and Geophysics, Chinese Academy of Sciences. Blue squares show MT stations of Bai et al. (1993a,b). The white dots are MT stations from this study. The black dots, squares and rectangles indicate the locations where the sharp variation in lithospheric thickness occurs. (b) S-wave velocity structure on the NCISP VI profile (Li and He, 2011). (c) 2-D resistivity model derived in this paper. (d) S-wave velocity image along NCISP III. The black dash lines in (b), (c), and (d) represent the variation of the lithospheric thickness along profile. Red ellipses mark the locations where the lithospheric thickness changes sharply. (For interpretation of the references to color in this figure legend, the reader is referred to the web version of this article.)

greater than the mantle transition zone, with low velocity anomalies due to temperature variation and/or partial melting. A new high-resolution 3-dimensional density model for the NCC was constructed from gravity data by Li and Yang (2011). This showed that three main units of the NCC have significantly different density structure, reflecting different tectonic histories in the Phanerozoic.

Limited MT studies have taken place in the study area. The first MT profile was recorded by Lu and Xia (1993) and detected low resistivity crustal layers and a change in electrical resistivity across the TLFZ. Bai et al. (1993a,b) reported a low resistivity anomaly that was interpreted as the suture zone between the CAOB and NCC (Fig. 3a).

In summary, the previous seismic studies indicate that a heterogeneous upper mantle with a thinned lithosphere is present beneath the NCC. Prior MT data were not able to image the upper mantle, which is a key feature for understanding the tectonic evolution. The long-period MT data presented in this paper are the first to image the mantle in this region.

3. Magnetotelluric data collection and processing

The magnetotelluric (MT) technique is a passive electromagnetic method that determines subsurface resistivity structure by measuring the time variation of natural electromagnetic fields at the Earth's surface (Chave and Jones, 2012). Lower frequencies (longer periods) penetrate deeper into the Earth, so measurements at a range of frequencies allow the variation of resistivity with depth to be determined. In this study, MT data were collected in 2011–2012 by the China Earthquake Administration at 48 stations with a typical spacing of 25 km. Broadband MT (BBMT) data for crustal imaging were recorded at every station using Phoenix Geophysics MTU5A instruments. Half of the BBMT stations recorded data for 24 h giving MT data in the range of 0.003–1000 s. The other half of the stations recorded for 72 h giving data in the range of 0.003–6000 s. The BBMT time series data were processed using the statistically robust algorithm of Egbert (1997) and mutual remote referencing. To provide deeper imaging, long period (LMT) data were recorded at 11 stations (Fig. 1) using LEMI systems. The LMT stations recorded for 3–4 weeks with a 1 Hz sampling rate, and were processed with the algorithm of Varentsov et al. (2003) to give data in the period range 10–30,000 s. At stations where both BBMT + LMT data were recorded, the data were merged to obtain responses in the period range 0.003–30,000 s. Most stations had good quality MT data, but the data quality was lower in the southeast part of the profile because of the higher population density and electrical noise caused by the DC electricity supply to mines.

4. Dimensionality and geoelectric strike direction

Before MT data can be used to generate a resistivity model, it is essential to determine if a 1-D, 2-D or 3-D approach is needed. The station layout was designed with the intention of using a 2-D analysis, with the profile location based on a strike direction inferred from regional geological structures. However, this orientation needs to be confirmed as part of the MT data analysis. Since the MT profile is long and crosses several geological provinces, it is possible that a single strike direction will not be applicable to the entire transect. Tensor decomposition is widely used to determine strike directions and remove galvanic distortion from MT data and was used in this study (Groom and Bailey, 1991). The measured impedance tensor is decomposed into a 2-D regional impedance tensor and a frequency-independent matrix that describes the galvanic distortion. The galvanic distortion is characterized by three terms: an anisotropy term, twist angle and shear angle.

Fig. 4 shows the results of tensor decomposition implemented with the algorithm of McNeice and Jones (2001). The red and blue wedges in the rose diagrams indicate the two possible strike directions. At short periods (1–10 s) there is significant scatter, but N45°E is the most commonly encountered value. A similar angle was also observed in the 10–100 s band. The strike angle is not clearly defined in the band 100–1000 s, but it returns to a well-defined value of N30°E in the band 1000–10,000 s. The geoelectric strike directions are also illustrated in map view in Fig. 4, with the length of line indicating the maximum phase difference observed as the impedance tensor is rotated. This quantity gives a measure of how non 1-D the MT impedance data can be considered. A large phase split indicates 2-D or 3-D resistivity structure. Tensor decomposition assumes that the regional structure is 2-D, and it is important to evaluate the validity of this assumption by examining the root-mean-square (r.m.s.) misfit of the decomposition model. This value is displayed as the color of the lines in Fig. 4 and misfit values below 2–3 indicate a satisfactory fit, implying that a regional 2-D impedance exists. The twist and shear angles quantify the degree of galvanic distortion and are small at most stations. Based on the results of tensor decomposition, the MT responses of most sites are consistent with a 2-D assumption. Although the geoelectric strike direction observed varies with different tectonic units, a consistent strike direction of N30°E or N60°W is observed at different periods. Note that there is an inherent ambiguity of 90° in the strike angle determined from tensor composition which can be resolved with geological information. In the study area, the dominant geological strike is about N30°E, which is consistent with the geoelectric strike direction estimated above.

The dimensionality was also analyzed using the phase tensor method (Caldwell et al., 2004), which is a useful because it makes no assumption about the regional dimensionality and is unaffected by galvanic distortion. Graphically, the phase tensor can be displayed as an ellipse that is defined by three invariants, the maximum phase (Φ_{max}), the minimum phase (Φ_{min}) and the skew angle (β). For a 2-D structure, the skew angle (β) is zero and either Φ_{max} or Φ_{min} occurs in the strike direction. However, when β is non-zero this indicates a 3-D resistivity structure. The phase tensor analysis is shown in Fig. 5, and large skew angles (>3°) at some sites may indicate relatively 3-D resistivity structure. The rose diagrams show the direction of the ellipse orientation, indicating the geoelectric strike direction. Although a range of directions are observed along the profile, the main axes of phase tensors at most sites are parallel to the regional geological strike. The phase tensor analysis favors a strike direction of N30°E to N45°E.

Induction vectors can also be used to investigate dimensionality and have the advantage that they do not have the 90° ambiguity encountered in tensor decomposition. In a two-dimensional (2-D) situation, the induction arrows are orthogonal to the geoelectric strike direction. It was found that the induction arrows were parallel to the profile at most sites in the NW part of the profile, but were quite scattered in the SE part of the profile due to strong cultural noise.

In summary, while there is scatter in the strike angles, N30°E to N40°E appears to be the most stable value based on tensor decomposition and phase tensor analysis. Since the mantle is the main focus of this paper, the strike direction determined from the lowest frequencies was preferred and a value of N35°E was chosen, which was consistent with the geological strike of major crustal structures such as the NSGL and TLFZ. The subsequent analysis considered variations of ±10° in this angle, and found that this did not significantly change the main features of the inversion model.
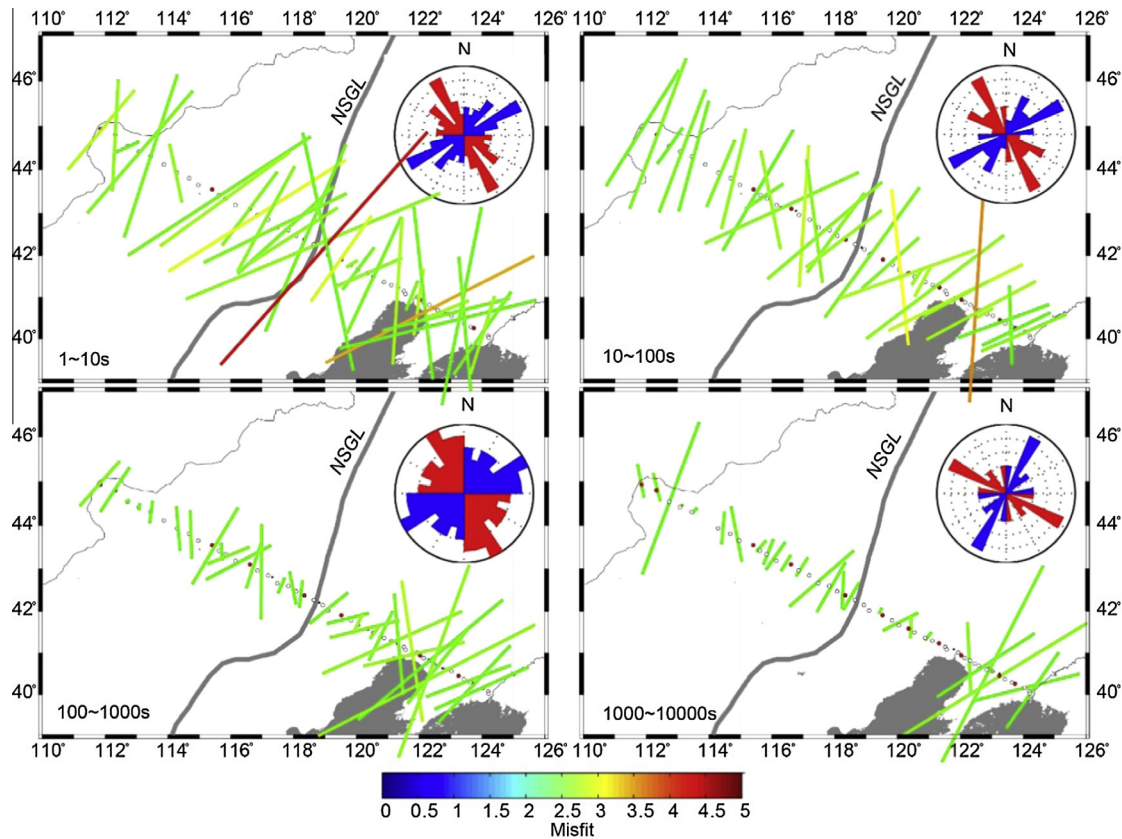
Fig. 4. Results of tensor decomposition. The color scale represents the r.m.s. misfit between the observed MT responses and the 2-D decomposition model. Blue and red wedges correspond to the two solutions for strike direction and reflect the 90° ambiguity in tensor decomposition. The ambiguity was resolved using the regional geological structure, with the preferred geoelectric strike direction plotted as the blue wedge. (For interpretation of the references to color in this figure legend, the reader is referred to the web version of this article.)

5. Magnetotelluric data

If a two-dimensional (2-D) resistivity structure is present, then MT data can be decomposed into the transverse electric (TE) mode and transverse magnetic (TM) mode by rotating the impedance tensor into the regional geoelectric strike direction. In the TE mode, electric currents flow parallel to the strike direction, while in the TM mode the current flows perpendicular to the strike direction. The apparent resistivity and phase curves at representative stations are shown in Fig. 6, after rotation to an azimuth of N35°E. At most stations, the phase angles are consistent with the apparent resistivity, with phases less than 45° occurring when apparent resistivity increases with period, and vice versa. The curves show significant variations along the profile, but a common feature at many sites is the presence of phases greater than 45° at the longest periods, indicating a decrease in resistivity at depth.

Fig. 7 shows pseudosections for MT data in the N35°E coordinate frame. The vertical stripes in the apparent resistivity pseudosections are due to static shifts, which are the results of shallow resistivity structure that change the magnitude of apparent resistivity at all frequencies and are also a form of galvanic distortion (Jones, 1988). These shifts need to be accounted for in MT data analysis as they can bias estimates of true resistivity and depths in resistivity models. The phase is not influenced by these shifts, resulting in smoother pseudosections. The phases are greater than 45° in both modes at periods greater than 100 s near the Xilamulun Fault (sites 14, 15, 16) and near the North South Gravity Lineament (sites 21, 22, 230). Additionally, high phases are observed around the TLFZ at sites 35, 36, and 37. These phases are an indication of low resistivity layers at depth.

6. 2-D magnetotelluric inversion and sensitivity tests

MT data quality was assessed using the D+ algorithm of Parker and Booker (1996) as implemented in the WinGlink software package. Data points with inconsistent apparent resistivity and phase, large scatter, and out of quadrant phases were deleted. The 2-D inversion was implemented using the algorithm of Rodi and Mackie (2001). MT data are never exactly 2-D, so an experimental approach was used to determine which subsets of the data (TE-mode, TM-mode, tipper) were mutually consistent. Since the different modes have sensitivity to different depth ranges and model features, it is optimal to include as much data as possible in a 2-D inversion. The TE-mode is inherently sensitive to 3-D effects caused by along strike features, and must be included with care (Wannamaker et al., 1984; Berdichevsky et al., 1998; Tauber et al., 2003; Ledo, 2006; Unsworth et al., 2004; Jones, 2006). An acceptably smooth model was found that fitted the TE mode, TM mode and T_{zy} data over the period range 0.001–10,000 s. Note that T_{zy} is the projection of the induction vector parallel to the profile, and is orthogonal to the strike direction in a 2-D situation.

The inversions were started from a uniform half-space of 100 Ω m with a mesh comprised of 126 columns and 131 rows. Since MT inversion is a non-unique process, regularization is widely used to apply a constraint to the inversion. The most common form of regularization is spatial smoothing. There is an inherent trade-off between the competing requirements of (a) fitting the measured MT data as closely as possible, while risking that the model becomes rough and contains artifacts and (b) having a smooth model that does not fit all features in the data. This trade-off can be quantified in the NLCG6 algorithm with the regu-
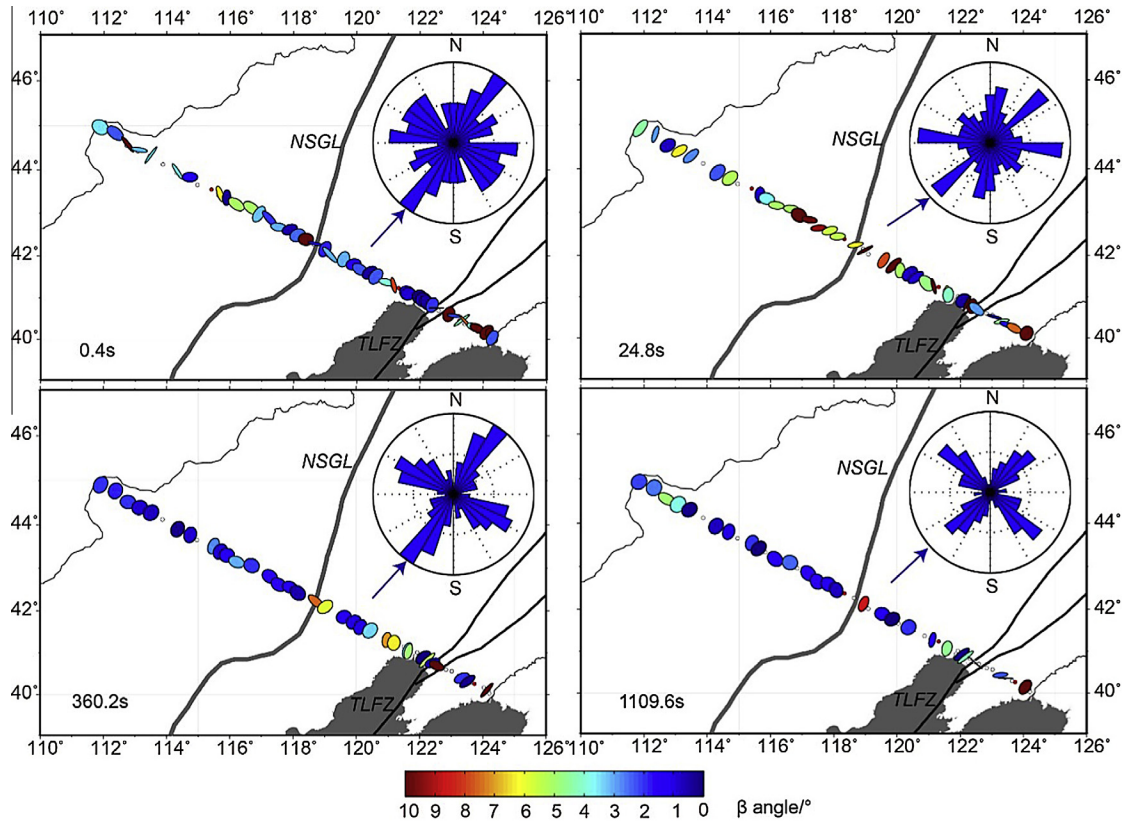
Fig. 5. Phase tensor ellipses, and colors represent the skew angle β. The rose diagrams represent the angle α–β, indicating the geoelectric strike direction. The blue arrows for each period represent the preferred strike directions. (For interpretation of the references to color in this figure legend, the reader is referred to the web version of this article.)

larization factor, τ, and inversions were performed with values of τ in the range of 0.3–1000. An optimal value of τ = 3 was determined by analyzing the L-curve (Booker et al., 2004; Farquharson and Oldenburg, 2004), as shown in Fig. 8. Another parameter used to control the regularization in the NLCG6 code is α, which controls the balance of vertical to horizontal smoothing in the resistivity model.

A significant number of inversions were implemented with different combinations of the control parameters. The final model used the parameters τ = 3, α = 1, and the inversion was allowed to compute static shifts coefficients for the TE mode and TM mode data. The error floors were set to 10% for the TM apparent resistivity, 5% for TM and TE phase (equivalent to 1.4°) and an absolute value of 0.05 for T_{zy}. To account for possible 3-D distortion, a higher error floor (20%) was applied to the TE apparent resistivity. Using these parameters, the inversion produced the model shown in Fig. 9 that had a final r.m.s. misfit of 2.57 after 200 iterations. The fit of the inversion model responses to the measured MT data is acceptable, as shown in both Figs. 6 and 7. Note that long-period MT data were only recorded at 8 stations.

Sensitivity tests were carried out in order to justify whether key features in the 2-D inversion model were required by the data, and investigated two low resistivity anomalies labeled 'A' and 'B' in Fig. 9. This was achieved by editing the resistivity model, and then restarting the inversion with the resistivity of the edited region fixed. For the Conductor 'A' beneath the XLML fault, the resistivity was changed to 500 Ω m, which is comparable to the resistivity on each side of this feature. It is clear that the change in the model causes an increase in apparent resistivity and a decrease in the phase, especially at site 14 and gives evidence that this feature is required by the MT data (Fig. 10). The same method was used to investigate the conductor 'B' which is located beneath the TLFZ,

and Fig. 11 shows that significant changes in apparent resistivity and phase have resulted. Therefore, the sensitivity test results indicate that low resistivity zones A and B are required to explain the measured MT data.

7. Interpretation and discussion

After multiple inversions and model validation, the resistivity model shown in Fig. 9 was selected as the preferred model. The model exhibits a number of distinct electrical resistivity features that correlate with the different tectonic provinces. To the northwest, the crust and upper mantle of the CAOB are characterized by relatively high resistivity values (100–1000 Ω m), while lower values (10–100 Ω m) are observed beneath the southeast section of the profile beneath the NCC. These resistivity variations can be interpreted by integration with previous geophysical and geological studies, as discussed in the next section and summarized in Fig. 12. Due to the relatively large inter-station spacing, it was not possible to image small scale resistivity features within the upper crust. Therefore the focus of the interpretation is on the deeper parts of the resistivity model.

7.1. Crustal structure

The crustal thickness within the region of the CAOB sampled by the MT profile is 38–40 km (Lu and Xia, 1993; Li et al., 2013). Within the NCC thickness varied from 40 km beneath the northern YSB to just 25 km beneath the TLFZ (Zheng et al., 2007b; Tang and Chen, 2008; Wei et al., 2011). As noted above, the MT station spacing is relatively large and not optimal to give detailed images of upper crustal structure. Nevertheless, a number of distinct anomalies are discernible and discussed below.
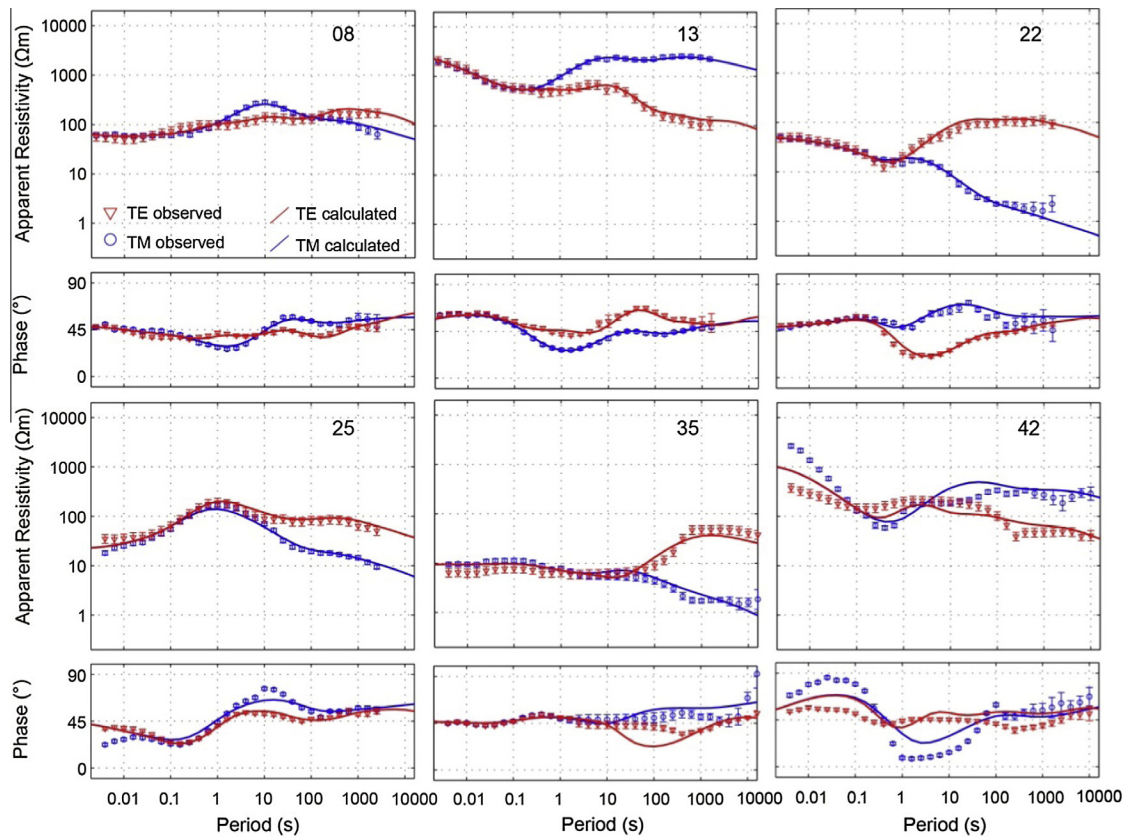
Fig. 6. Examples of MT responses at six sites along the profile. The data were rotated to the N35°E geoelectric strike direction. Solid lines show the 2-D responses of TM mode (blue) and TE mode (red). (For interpretation of the references to color in this figure legend, the reader is referred to the web version of this article.)

Along most of the profile, the upper crust has a high resistivity (>300 Ω m) that is likely due to crystalline basement rocks (BGMRLP, 1989; BGMRIM, 1991). Zones of low resistivity are observed at the surface where the profile crosses the shallow sedimentary basin near the TLFZ. A lower crustal conductor can be detected in several areas, as is often the case in crustal MT studies (Haak and Hutton, 1986) and appears particularly strong beneath the NSGL.

A number of low resistivity pathways extend through the crust. Those imaged close to the southeast end of the MT profile and may represent fluid pathways from the upper mantle with elevated porosity owing to ongoing deformation in this region. In the Northwest part of the profile, within the CAOB, a conductor appears to be associated with the Solonker suture, which was formed in the late Permian by the collision of the NCC and Siberian Craton (Xiao et al., 2003; Jian et al., 2010). Resistivity models derived from MT data can sometimes image suture zones, e.g. a dipping high conductivity layer was found in the Iapetus Suture Zone in Ireland and was interpreted as a layer of sulfide-bearing graphitic sediments deposited during the closure of the Iapetus Ocean (Rao et al., 2007). Aqueous fluids cannot explain the low resistivity as they will not remain in the crust over timescales of hundreds of millions of years without some mechanism for recharge. In the present study, a crustal conductor is imaged in the region of the Solonker suture (station 8–10) and appears to dip northwest, consistent with the proposed subduction direction. However the broad station spacing means that it cannot be reliably traced to the surface.

7.2. Upper mantle resistivity structure

Fig. 9 shows that the crustal and upper mantle resistivity varies systematically from northwest to southeast along the profile. Over-

all, the upper mantle beneath the CAOB exhibits a relatively high resistivity (300–1000 Ω m) compared to the NCC upper mantle, where the resistivity is lower (100 Ω m). Seismic studies have shown that the lithospheric thickness varies along the profile from 120–150 km beneath the CAOB, to around 100 km beneath the NCC (Fig. 12; Li and He, 2011).

7.2.1. Composition of upper mantle beneath the CAOB

In the northwestern part of the profile beneath the CAOB, high resistivity values (300–1000 Ω m) extend to depths of 200 km, consistent with a thick lithosphere. Interpretations of the electrical resistivity of the lithosphere can be ambiguous. For instance, low resistivity can be interpreted in terms of several conduction mechanisms that include hydrous silicate minerals, partial melt, aqueous fluids or conductive phases such as graphite and metallic oxides (Pommier, 2014). This non-uniqueness can be reduced by laboratory studies (Selway, 2014). Detailed interpretations of upper mantle resistivity have been published for cratonic regions including the Archean Kaapvaal Craton and the Proterozoic Rehoboth Terrane, South Africa (Jones et al., 2009, 2012; Fullea et al., 2011) the Slave Craton in Northwest Canada (Jones et al., 2005; Ledo and Jones, 2005) and the Tanzanian Craton (Selway et al., 2014). Studies in active regions have been published for back arc regions such as the southern Canadian Cordillera (Rippe et al., 2013). It is often observed that the resistivity of the upper mantle is less than predicted by a dry olivine composition. A key point to address is whether this decrease in resistivity is due to the presence of partial melt, water (hydrogen), graphite or sulfides.

The presence of water or partial melt in the CAOB upper mantle was investigated with the approach of Rippe et al. (2013) shown in Fig. 13. Small amounts of water (hydrogen) dissolved in minerals such as olivine can significantly reduce their electrical resistivity
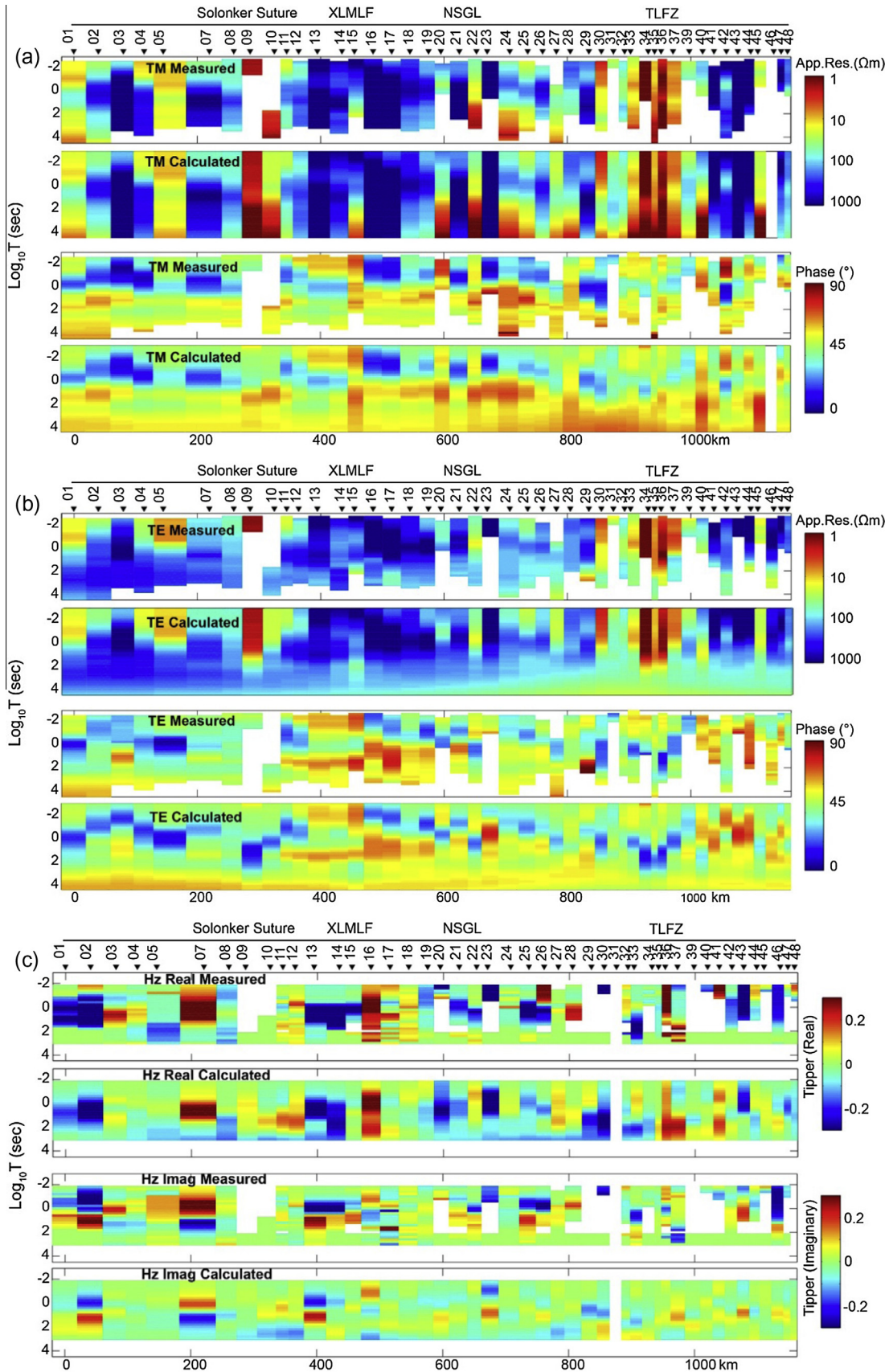
Fig. 7. (a) Measured and calculated pseudosections of apparent resistivity and phase for the TM mode. (b) Measured and calculated pseudosections of apparent resistivity and phase for the TE mode. (c) Measured and calculated pseudosections of real and imaginary parts of the vertical magnetic field transfer function.
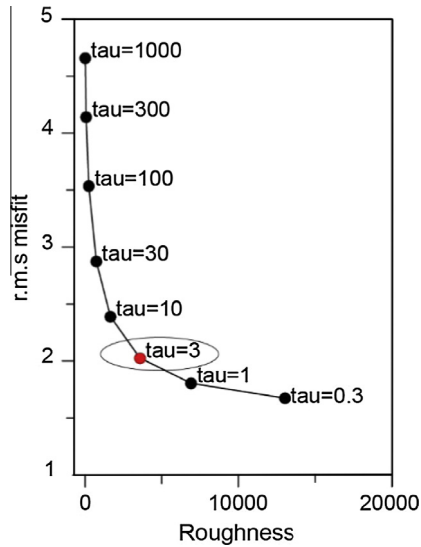
Fig. 8. Graph illustrating the trade-off between the data r.m.s. misfit and the model roughness. Tau = 3 was chosen for the final model.

(Karato, 1990; Wang et al., 2006; Yoshino et al., 2009). However, experiments by various groups give differing estimates for the decrease caused by a given amount of water and one model was recently updated (Yoshino et al., 2014). The primary input is the resistivity model derived from the MT inversion (Fig. 13a). To illustrate the sensitivity of the analysis, calculations were also performed for a resistivity that is double, and half, of the value from the 2-D inversion. The secondary input is the temperature, and values from Sun et al. (2013) were used (Figs. 12e and 13b). The temperature is below the peridotite dry solidus at all depths, as expected. The third column (Fig. 13c) shows the water content required to explain the observed resistivity at station 4 on the CAOB. This calculation was performed using the results of both Wang et al. (2006) and Yoshino et al. (2009).

The H^+ content exceeds the solubility limit (Lizarralde et al., 1995) at depths shallower than 55 and 65 km for the Wang/Yoshino models respectively. Above this depth, $H+$ cannot explain the

observed upper mantle resistivity and there are three distinct possibilities for the low resistivity:

(a) Graphite films. Carbon will be present as graphite at depths above the graphite–diamond stability field, which occurs around 140–150 km at the elevated temperatures encountered in NE China (Kennedy and Kennedy, 1976). However recent laboratory studies suggest that the interconnection needed to produce the low resistivity will not occur above 700 °C (Yoshino and Noritake, 2011). This depth occurs at 30–40 km in NE China (Fig. 14) and suggests that the upper mantle is too hot for this conduction mechanism to cause the observed low resistivity.

(b) Sulfide minerals. These have been suggested as a possible cause for low resistivity zones in the upper mantle (Jones et al., 1997; Ducea and Park, 2000; Jones and Craven, 2004). Laboratory measurements have shown that approximately 1% volume fraction of iron sulfides can lower the bulk resistivity, so sulfide minerals are a possible explanation for the resistivity of the upper mantle beneath the CAOB.

(c) Partial melting. The presence of water (H+) will lower the melting point of olivine. Fig. 13c shows the water concentration in wt-% needed to lower the melting point to that of the observed geotherm and initiate melting. It can be seen that partial melting could occur above a depth of 55 km (Wang) and above 65 km (Yoshino). At depths less than 55–65 km the observed resistivity could be due to a combination of partial melt and water – it is not possible to determine the combination of melt/water, so Fig. 13d shows the maximum melt fraction. In this calculation, the overall resistivity was computed using the modified Archie's Law of Glover et al. (2000) for two conducting phases with a melt resistivity of 0.2 Ω m. The required melt fraction is below 1% for both the Wang and Yoshino results. Note that the Wang results require melt above 50 km, while the Yoshino results require melt above 70 km.

Below a depth of 55–65 km depth, hydrogen alone can explain the observed resistivity in the upper mantle, and no partial melt is needed. The Wang/Yoshino results predict a water content up to
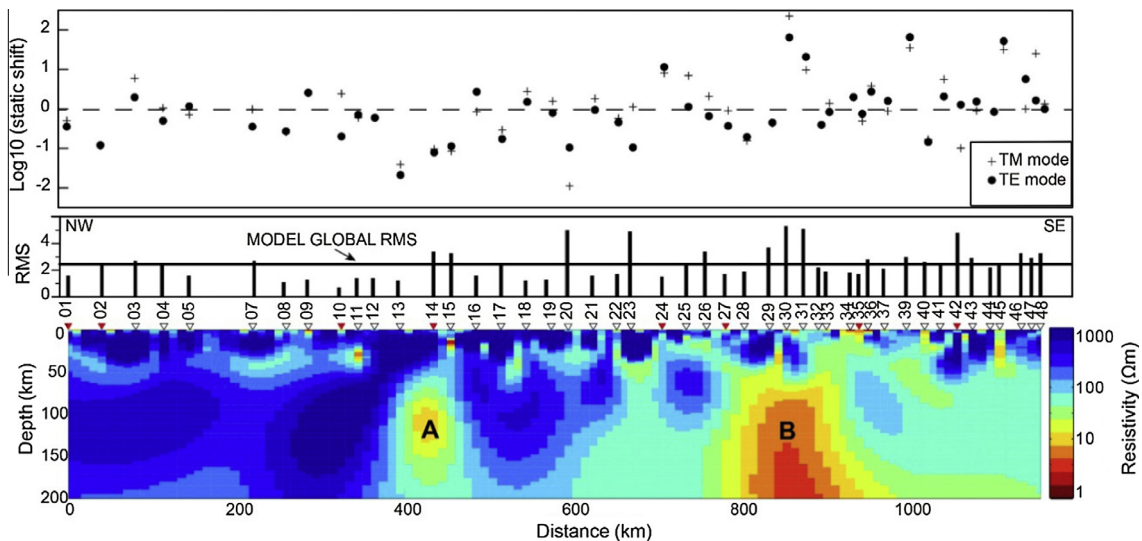

Fig. 9. Upper panel shows the static shift coefficients for the TE and TM mode data in the inversion; Middle panel shows RMS misfit at each site; Lower panel represents the final 2-D resistivity model obtained from the joint inversion of the TM, TE and T_{zy} data. Sites with BBMT and LMT data are represented by red triangles, sites only with BBMT data by white triangles. The labeled anomalies A, B are discussed in the text and following figures. (For interpretation of the references to color in this figure legend, the reader is referred to the web version of this article.)
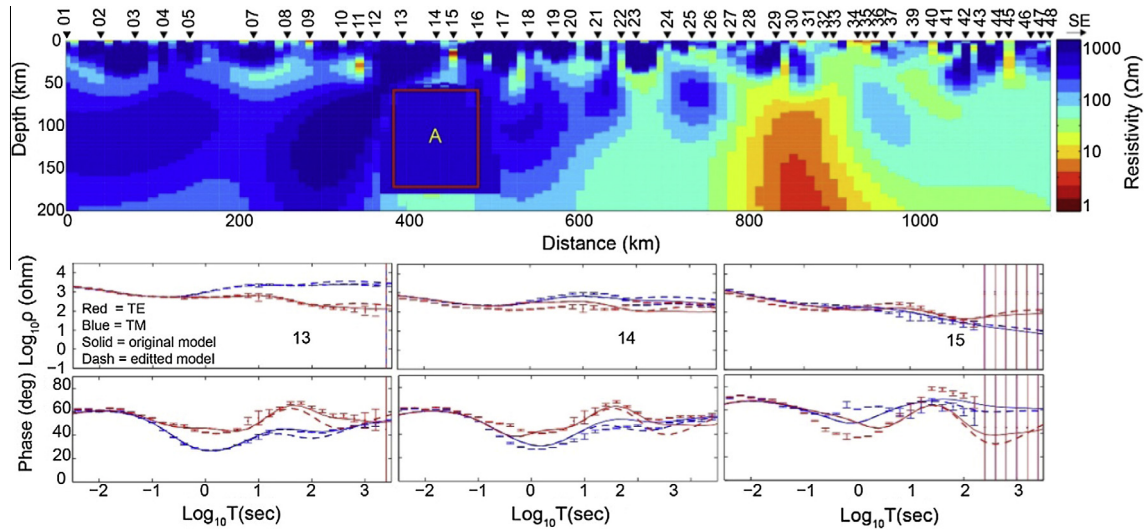
Fig. 10. Upper panel shows the edited resistivity model fixing the anomaly A with a resistivity value of 500 Ω m. Lower panel shows the comparison between the measured MT data and responses from the original model and the edited model inversion at station 13, 14, 15.
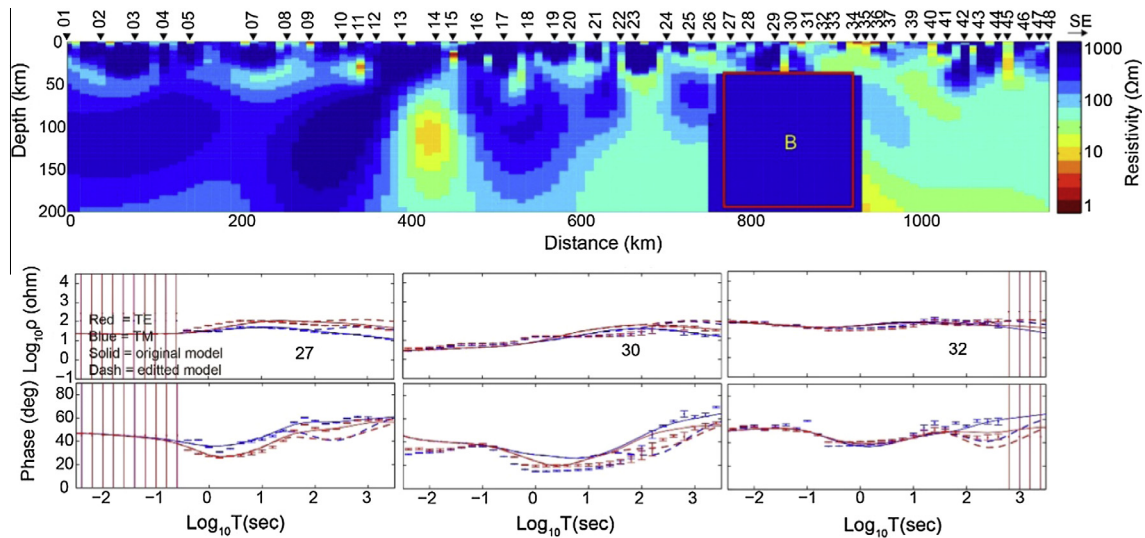

Fig. 11. Upper panel shows the edited resistivity model fixing the anomaly B with a resistivity value of 500 Ω m under the TLFZ. Lower panel shows the comparison between the measured data and responses from the original model and the edited model inversion at station 27, 30, 32.

0.08–0.1 wt-% respectively, which can be expressed as 800–1000 weight ppm water. These water contents are similar to those obtained from xenolith studies of cratons (Peslier et al., 2010; Doucet et al., 2014) and inferred from MT studies (Selway et al., 2014). These values are relatively high and indicate that the lithospheric mantle has been hydrated beneath the CAOB.

7.2.2. Composition of upper mantle beneath the NCC

The composition of the NCC upper mantle was investigated using the same approach as for the CAOB. Note that temperatures at 100 km depth are more than 100 °C higher than beneath the CAOB. At site 42 in the NCC, the electrical resistivity shows a decrease with depth from 200 Ω m at 40 km to 50 Ω m at 100 km.

At depths less than 70–80 km, the water content required to explain the observed resistivity exceeds the water solubility limit. As in the CAOB, an elevated water content cannot explain the resistivity of the uppermost mantle, and an alternative explanation is needed. Temperatures may be too high for graphite films to remain connected over geological timescales, and sulfide minerals or par-

tial melt are possible explanations. As shown in Fig. 13d, the elevated temperature beneath the NCC indicates that the water content predicted by both the Wang et al. (2006) and Yoshino et al. (2009) models is sufficient to allow for hydrous melting in the upper mantle, to depths of at least 100 km and melt fractions between 0.2% and 1% are required (Fig. 13d).

In the deeper part of the model, the water content at 70 km is 0.1–0.15 wt% based on the models of Wang et al. (2006) and Yoshino et al. (2009) respectively. These values decrease to 0.01–0.05 wt% at 100 km depth. These values are below the water solubility limit, indicating that water alone can explain the observed mantle resistivity.

In summary, the uppermost mantle (down to 70–80 km) of the NCC likely contains a combination of water and partial melt. At greater depths it only requires water, with a water content of 0.05 wt% estimated at 100 km depth (equivalent to 500 ppm). Xenolith studies can be used to give an independent estimate of water contents. Basalts erupted during craton destruction in the Mesozoic, are characterized by high water contents that exceed
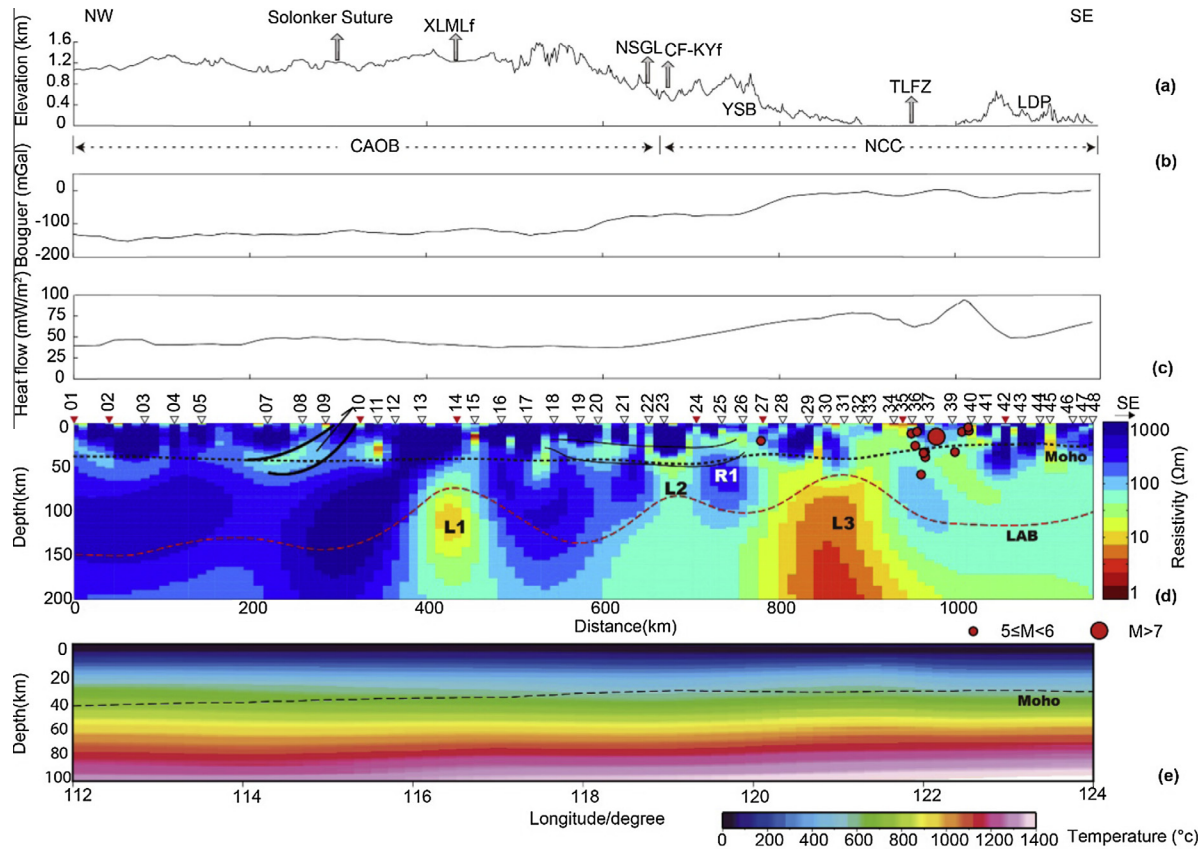
Fig. 12. (a) Topography from the Shuttle Radar Topography Mission (SRTM) database (b), Bouguer gravity anomaly from the Earth Gravitational Model (EGM2008) database (c) surface heat flow from the global heat flow database of the International Heat Flow Commission (d) 2-D resistivity model along profile. XLMLf: Xilamulun fault; CF-KYf: Chifeng-Kaiyuan fault; TLFZ: Tanlu Fault Zone; LDP: Liaodong Peninsula; YSB: Yansha Belt; CAOB: Central Asian Orogenic Belt; NCC: North China Craton. L1, L2, L3 are corresponding to three different low resistivity zones. R1 represents a high resistivity zone. The dashed black line represents the location of the Moho based on Lu and Xia (1993) and Wei et al. (2011). The dashed red line shows the boundary between the lithosphere and the asthenosphere following Lu and Xia (1993), Li and He (2011) and Wei et al. (2011). Hypocenters taken from China Earthquake Networks, Seismic Data Management and Service System. (e) Temperature along the profile from Sun et al. (2013). The dashed line denotes the Moho (from Crust 2.0 model) (http://igppweb.ucsd.edu/~gabi/crust2.html) (Bassin et al., 2000). (For interpretation of the references to color in this figure legend, the reader is referred to the web version of this article.)

1000 ppm (Xia et al., 2013) perhaps due to the subduction since the early Paleozoic. However, peridotite xenoliths from the eastern part of the NCC show a broad variation in water content (Xia et al., 2010; Wang et al., 2014) that was proposed to be the result of dehydration caused by heating by upwelling asthenosphere flow that acted in concert with NCC lithospheric thinning during the late Mesozoic to early Cenozoic. Yang et al. (2008) report water contents up to 100 ppm in NCC peridotites and 100–1000 ppm in granulites, indicating that the water distribution is quite heterogeneous and may result in spatial variability in rheology. Overall, xenolith studies give strong evidence for high, but spatially variable, water content in the NCC upper mantle.

The values of 500 ppm at depths of 100 km are higher than the low values (10 ppm) required to give the high strength required for craton longevity (Peslier et al., 2010). They are higher than the elevated values of 100 ppm reported by xenolith studies on the Kaapvaal craton (Peslier et al., 2010) and a value of 100 ppm was inferred from MT data in the Tanzanian Craton (Selway et al., 2014). The high values from the NCC are closer to the values reported by Doucet et al. (2014) in xenoliths in the Siberian Craton (300 ppm). These values suggest that the lithosphere of many cratons may not be as dehydrated as previously believed. In the case of the NCC, this water was likely transported into the upper mantle by the subducting Pacific Plate and would have initiated melting of the back arc upper mantle, and lowered the mantle viscosity (Karato and Wu, 1993; Dixon et al., 2004) allowing water to be

distributed throughout the back-arc upper mantle and lithospheric thinning/craton destruction to occur.

Mantle xenoliths from the Colorado Plateau and vicinity from the North America Craton have also revealed elevated water contents (Li et al., 2008) and suggest that a similar process occurred when the Farallon plate was subducted beneath North America during the early Cenozoic. The elevated water contents would have caused the hydration and weakening of the cratonic mantle and led to the observed lithospheric thinning.

7.2.3. Low resistivity anomalies

The MT data show that the resistivity of the lithosphere does not change smoothly across this region. Two major zones of low resistivity are observed (L1 and L3), and it was demonstrated that these features were required by the measured MT data. A smaller zone of low resistivity, L2, was also detected. Since these features may be related to ongoing deformation, it is important to determine the physical cause of the low resistivity by considering the topography, Bouguer gravity anomaly and heat flow (Fig. 12) and the seismic sections (Fig. 3).

7.2.3.1. L1 – Xilamulun fault (XLML-f). The low-resistivity anomaly L1 appears at >80 km depth beneath the surface trace of the Xilamulun fault (XLML-f) as shown in Fig. 12. The resistivity of L1 is too low to be explained by hydrogen diffusion in olivine and requires either partial melt or an increased concentration of sulfide miner-
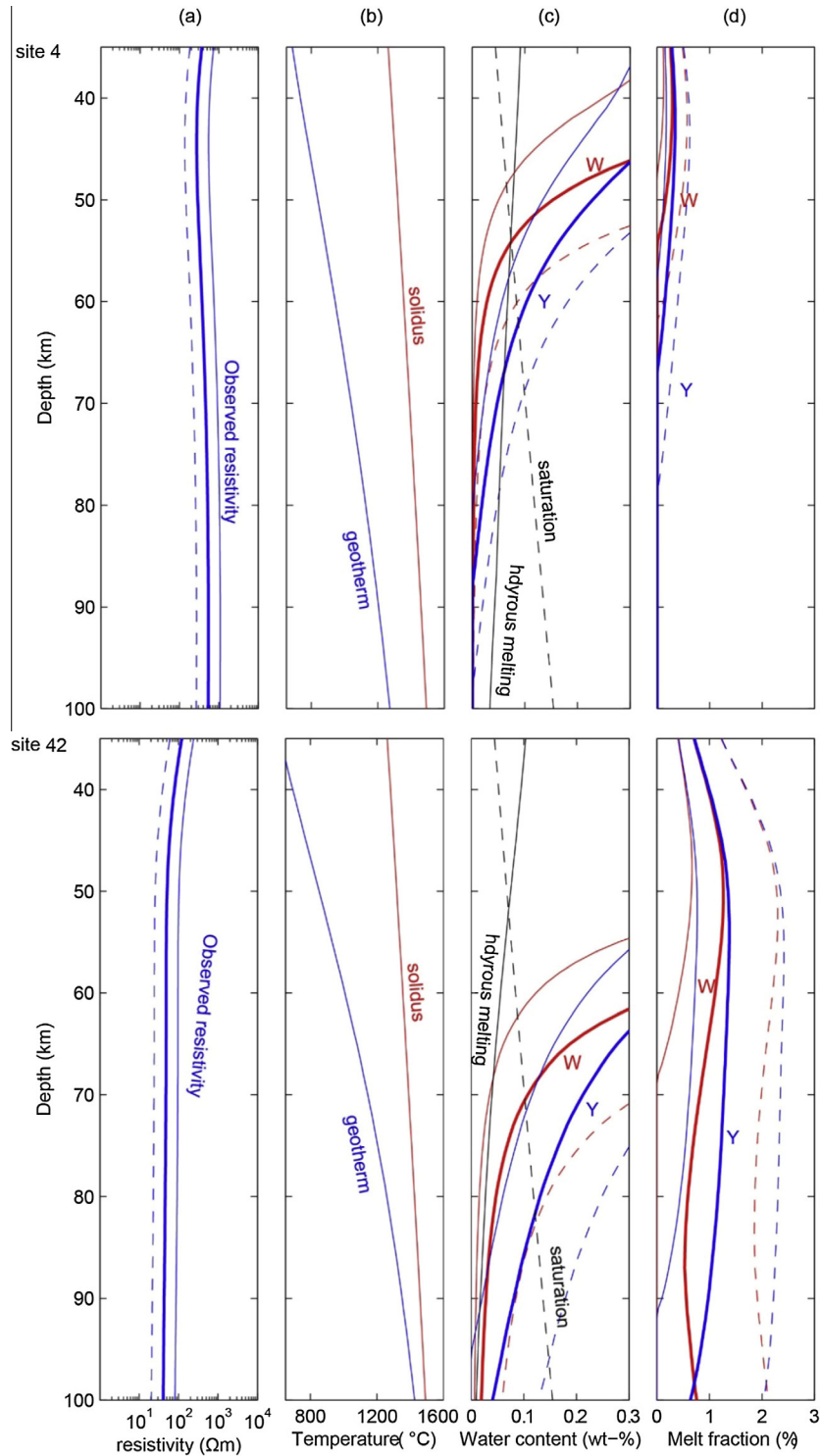
Fig. 13. Electrical resistivity, mantle temperature, water content and melt fraction for two stations along profile: site 4 in the Central Asian Orogenic Belt; site 42 in the North China Craton. From left to right: (a) Resistivity obtained from MT inversion (thick blue line). Resistivity multiplied by 0.5 (thin blue dashed line) and multiplied by 2 (thin blue line). (b) Geotherm (blue line) and dry peridotite solidus (red line). (c) Water content calculated from the results of Wang et al. (2006) and the MT inversion (thick red line). The thin red lines show the water content when the inversion model resistivity is multiplied by 2 and 0.5. The blue lines show the water content calculated using the results of Yoshino et al. (2009). Water content required for hydrous melting (black solid line). Water solubility limit (black dash line). (d) Melt fractions calculated using the results of Wang et al. (2006) are shown with the thick red line. Thin red lines show the melt fractions when the resistivity from the inversion model is multiplied by 0.5 and 2. Blue lines show the melt fractions calculated with the results of Yoshino et al. (2009). (For interpretation of the references to color in this figure legend, the reader is referred to the web version of this article.)

als or graphite. However, graphite films will not remain connected over geological timescales (Yoshino and Noritake, 2011). Consequently, partial melt could be a plausible explanation for the low

resistivity of L1. In addition, sharp lateral resistivity variations are observed here, indicating that the lithosphere under the Xilamulun fault is thinner than on either side. This is consistent with the
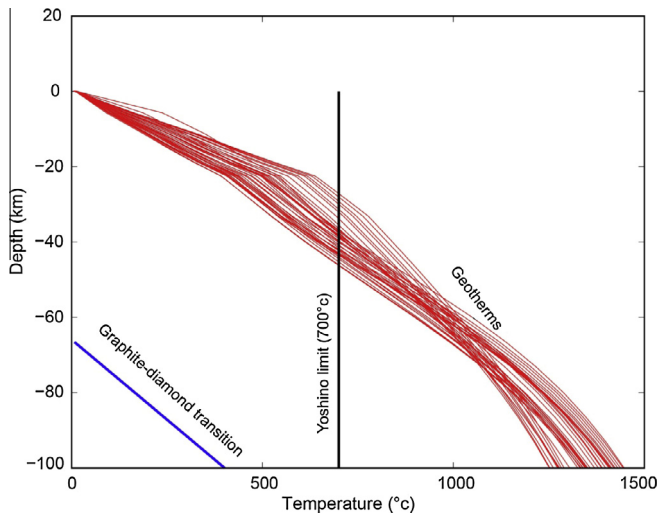
Fig. 14. Temperature–depth relationship for 48 stations along profile. Blue line shows the graphite–diamond transition boundary (Kennedy and Kennedy, 1976). Blue line represent the temperature at which the graphite will become unstable. (For interpretation of the references to color in this figure legend, the reader is referred to the web version of this article.)

seismically detected LAB undulation shown in Fig. 12d (Lu and Xia, 1993; Li and He, 2011). A significant change in magnetic anomaly was also observed in this region (Lu et al., 1993) perhaps associated with a change in Curie depth.

It has been suggested that the Xilamulun fault is an important tectonic zone, along which intense deformation, magmatic activity and associated mineralization occurred (Davis et al., 2002). Based on the resistivity model, together with other geophysical and geological observations, it is proposed that the Xilamulun fault is associated with a major litho-tectonic boundary that has a significant effect on the structure and composition of the lithosphere in this region.

7.2.3.2. L2 – North–South Gravity Lineament (NSGL). Thinned lithosphere near the NSGL was inferred from observations of crustal low resistivity and low velocity (Bai et al., 1993a,b; Tang and Chen, 2008; Wei et al., 2011; Li and He, 2011). Taking into account the higher temperature at this depth, partial melt is the most likely explanation for the low resistivity of L2. It has been proposed that the NSGL might represent the boundary between two tectonic regimes, with back-arc extension related to Pacific subduction to the east and convergence due to the Indo-Eurasian collision to the west (Xu, 2007). The model presented in this paper suggests that the NSGL is a lithospheric-scale boundary that has played an important role in lithospheric thinning. The strike direction of the NSGL (N30°E) is also significant. The boundaries of the Solonker suture and related features strike east–west. Since the initiation of subduction of the Pacific Plate beneath this region in the early Cretaceous (Kusky et al., 2007), the regional structural strike may have changed from N90°E to N30°E.

7.2.3.3. L3 – Tanlu Fault Zone (TLFZ). The third low resistivity anomaly is located beneath the TLFZ. High temperatures rule out graphite as a cause of the low resistivity. Seismic studies have reported a low velocity anomaly beneath the northern and southern TLFZ (Niu et al., 2000; Chen et al., 2006). Partial melt is the preferred explanation for observation of elevated heat flow (Fig. 12c) (Hu et al., 2000) and the coincident seismic and resistivity anomalies. Since partial melt lowers the strength of the crust and upper mantle, this observation has important implications for the dynamics of this region, since it implies that this feature might have acted as a

major channel for asthenospheric upwelling during the Mesozoic–Cenozoic continental extension and lithospheric thinning in eastern China.

7.2.4. Constraint on mechanism of lithospheric thinning

The resistivity model derived in this study shows two first order features in the lithospheric structure:

(1) **A decrease in upper mantle resistivity from Northwest to Southeast**. The resistivity decrease can be explained by a combined increase in temperature and partial melt and associated increase in the concentration of water – although sulfide minerals could also contribute to this change.

(2) **Discrete upper mantle conductors**. This decrease does not occur smoothly, and there are three regions of low resistivity in the upper mantle (L1, L2 and L3).

How can these observations contribute to the debate about the mechanism of lithospheric thinning? Models that have been proposed for lithospheric erosion can be grouped into two categories: (1) delamination, where parts of the lithosphere sink into the asthenosphere (Gao et al., 2004, 2008; Deng et al., 2007) and (2) asthenospheric erosion where hot upwelling material removes the base of the lithosphere (Zheng et al., 1998, 2007a; Xu et al., 2004). Some studies have proposed that destruction of the NCC has not been spatially uniform and characterized by localized zones of rapid destruction (Chen et al., 2006, 2008; Zhu and Zheng, 2009). The resistivity model presented in this study supports this type of destruction, based on the observation of conductors in the upper mantle adjacent to the NSGL and TLFZ. The low resistivity features within the NCC (L2 and L3) can be identified with zones of lithospheric erosion and the intermediate region of high resistivity in the upper mantle could be a region where delamination is occurring (R1). It should be noted that while the data presented in this paper do not cover the entire NCC, the heterogeneous resistivity structure is clearly present within the study area.

L2 is located near the NSGL, and likely caused by the presence of partial melt. The extensive magmatism in this region is recorded by the voluminous Mo–Cu ores of the Xilamulun metallogenic belt, and R1 could be the remnant of this magmatic activity. A lower heat flow above this high resistivity feature is consistent with this feature representing a pulse of past magmatism that is now cooling.

L3 underlies the eastern segment of the YSB and neighboring TLFZ and is characterized by lower resistivities than L2. This implies larger volumes of fluids are present, with partial melt as the preferred explanation for the low resistivity. It was previously suggested that the TLFZ was a weakened zone that experienced rapid extension and magmatism during the Mesozoic–Cenozoic (Zheng et al., 1998, 2008; Xu et al.,, 2004; Chen et al., 2006). The TLFZ existed before craton destruction began and cuts through the eastern NCC as a lithospheric scale fault system. This pre-existing structure may have provided a path for upwelling asthenospheric material (Zheng et al., 1998). It has been proposed that the mechanism of the lithospheric thinning beneath the YSB occurred by delamination (Gao et al., 2004; Deng et al., 2007), whereas thermal erosion dominated beneath the TLFZ (Zheng et al., 1998, 2007a; Xu et al., 2004; Zheng et al., 2008). It is proposed that the region L3 beneath between the YSB and the TLFZ may be the result of lithospheric thinning caused by a combination of delamination and thermal erosion. The TLFZ is associated with elevated heat flow, perhaps suggesting that this zone continues to be supplied with fluids/partial melt.

In summary, the resistivity images show evidence that lithospheric destruction beneath the eastern NCC has occurred in a spa-

tially non-uniform manner. The zones L1, L2 and L3 can be identified as regions of elevated fluid content that represent the location of upwelling, and which may continue into the future. Beneath the YSB the lithosphere appears to be resistive, and this could indicate intact lithosphere, which may be in the process of delaminating.

It should be emphasized that there can be other, non-fluid, explanations in Phanerozoic orogenic belts for the origin of low resistivity and low velocity anomalies (Lebedev et al., 2006; Shomail et al., 2006; Fishwick et al., 2008; Begg et al., 2009; Spratt et al., 2009). However, in the present study other geophysical, geochemical and petrological data have suggested that high heat flow and low lithospheric strength are characteristic of the region (Wang and Cheng, 2012; Chen et al., 2013). In combination with our resistivity model and calculated water contents, the preferred explanation is that the low resistivity observed within the study region is due to elevated concentrations of fluid.

8. Conclusions

An MT study of Northeastern China has revealed a number of features that are significant in terms of the tectonic evolution of the region.

The NW-dipping low resistivity zone in the crust beneath the Solonker suture zone confirms the location and polarity of this feature.

The MT data show that there is significant lateral variation in the electrical resistivity of the lithosphere in this region. The CAOB is characterized by relatively thick lithosphere with an upper mantle resistivity in the range 300–1000 Ω m, which can be explained by an elevated concentration of H+ (800–1000 wt ppm). This is in contrast to the thin, low resistivity lithosphere beneath the northeastern NCC. In this region, partial melts, or other conducting phases are needed to explain the observed upper mantle resistivity.

The change in lithospheric resistivity does not occur smoothly along the profile, and three low resistivity features suggest that the lithospheric thinning has occurred in a spatially non-uniform manner. The first is located under the Xilamulun fault and could be a lithospheric scale feature. The second is located near the NSGL and shows that this lineament is associated with a lithospheric scale resistivity feature. The third anomaly is close to the TLFZ, and the scale of this feature suggests that the TLFZ has played an important role in the Phanerozoic tectonic modification of the eastern NCC.

The models presented in this paper can address the questions posed in the introduction as follows. (1) The observed resistivity and the estimated water contents imply that the lithospheric mantle of the CAOB is hydrated to levels comparable to that of many cratons. The lower resistivity of the northeastern NCC requires elevated water contents and probably a small amount of partial melt, which will reduce the lithospheric strength. (2) The southeast decrease in upper mantle resistivity does not occur uniformly and a couple of major conductors are observed. These features could have originated from a combination of delamination and thermal erosion, and represent zones of inherent weakness that have continued to the present day.

References

Bai, D.H., Zhang, D.H., Kong, X.R., 1993a. A magnetotelluric study of the Paleozoic collision zone in the east of Inner Mongolia, I: observations and data analysis. Acta Geophys. Sin. 36, 326–336 (in Chinese).

Bai, D.H., Zhang, D.H., Kong, X.R., 1993b. A magnetotelluric study of the Paleozoic collision zone in the east of Inner Mongolia, II: two-dimensional modelling. Acta Geophys. Sin. 36, 773–783 (in Chinese).

Bassin, C., Laske, G., Masters, G., 2000. The current limits of resolution for surface wave tomography in North America. EOS Trans. AGU 81, F897.

Begg, G.C., Griffin, W.L., Natapov, L.M., O'Reilly, S.Y., Grand, S.P., O'Neil, C.J., Hronsky, J.M.A., Djomani, Y.P., Swain, C.J., Deen, T., 2009. The lithospheric architecture of Africa: seismic tomography, mantle petrology, and tectonic evolution. Geosphere 5, 23–50.

Berdichevsky, M.N., Dmitriev, V.I., Pozdnjakova, E.E., 1998. On two-dimensional interpretation of magnetotelluric soundings. Geophys. J. Int. 133, 585–606.

BGMRIM (Bureau of Geology and Mineral Resources of Inner Mongolia), 1991. Regional Geology of Nei Mongol (Inner Mongolia) Autonomous Region. Geological Publishing House, Beijing.

BGMRLP (Bureau of Geology and Mineral Resources of Liaoning Province), 1989. Regional Geology of Liaoning Province. Geological Publishing House, Beijing.

Booker, J.R., Favetto, A., Pomposiello, M.C., 2004. Low electrical resistivity associated with plunging of the Nazca flat slab beneath Argentina. Nature 429, 399–403.

Caldwell, T.G., Bibby, H.M., Brown, C., 2004. The magnetotelluric phase tensor. Geophys. J. Int. 158, 457–469.

Chave, A.D., Jones, A.G., 2012. The Magnetotelluric Method: Theory and Practice. Cambridge University Press, Cambridge.

Chen, L., 2009. Lithospheric structure variations between the eastern and central North China Craton from S-and P-receiver function migration. Phys. Earth Planet. Inter. 173, 216–227.

Chen, L., 2010. Concordant structural variations from the surface to the base of the upper mantle in the North China Craton and its tectonic implications. Lithos 120, 96–115.

Chen, L., Zheng, T.Y., Xu, W.W., 2006. A thinned lithospheric image of the Tanlu Fault Zone, eastern China: constructed from wave equation based receiver function migration. J. Geophys. Res. 111, B9312. http://dx.doi.org/10.1029/2005JB003974.

Chen, L., Tao, W., Zhao, L., Zheng, T.Y., 2008. Distinct lateral variation of lithospheric thickness in the Northeastern North China Craton. Earth Planet. Sci. Lett. 267, 56–68.

Chen, L., Cheng, C., Wei, Z.G., 2009. Seismic evidence for significant lateral variations in lithospheric thickness beneath the central and western North China Craton. Earth Planet. Sci. Lett. 286, 171–183.

Chen, L., Cheng, C., Wei, Z.G., 2010. Contrasting structural features at different boundary areas of the North China Craton and its tectonic implications. Adv. Earth Sci. 25, 571–581.

Chen, B., Chen, C., Kaban, M.K., Du, J.S., Liang, Q., Thomas, M., 2013. Variations of the effective elastic thickness over China and surroundings and their relation to the lithosphere dynamics. Earth Planet. Sci. Lett. 363, 61–72.

China Earthquake Networks Center, Seismic Data Management and Service System, 2013. <http://www.csndmc.ac.cn/newweb/index.jsp>.

Cipar, J., 1979. Source processes of the Haicheng, China, earthquake from observations of P and S waves. Bull. Seismol. Soc. Am. 69, 1903–1916.

Davis, G.A., Darby, B.J., Zheng, Y.D., Spell, T.L., 2002. Geometric and temporal evolution of an extension detachment fault, Hohhot metamorphic core complex, Inner Mongolia, China. Geology 30, 1003–1006.

Deng, J.F., Su, S.G., Niu, Y., Liu, C., Zhao, G.C., Zhao, X.G., Zhou, S., Wu, Z.X., 2007. A possible model for the lithospheric thinning of North China Craton: evidence from the Yanshanian (Jura-Cretaceous) magmatism and tectonism. Lithos 96, 22–35.

Dixon, J.E., Dixon, T.H., Bell, D.R., Malservisi, R., 2004. Lateral variation in upper mantle viscosity: role of water. Earth Planet. Sci. Lett. 222, 451–467.

Doucet, L.S., Pesiler, A.H., Ionov, D.A., Brandon, A.D., Golovin, A.V., Goncharov, A.G., Ashchepkov, I.V., 2014. High water contents in the Siberian cratonic mantle linked to metasomatism: an FTIR study of Udachnaya peridotite xenoliths. Geochim. Cosmochim. Acta 137, 159–187.

Ducea, M.N., Park, S.K., 2000. Enhanced mantle conductivity from sulfide minerals, southern Sierra Nevada, California. Geophys. Res. Lett. 27, 2405–2408.

Egbert, G., 1997. Robust multiple station magnetotelluric data processing. Geophys. J. Int. 130, 475–496.

Fan, W.M., Zhang, H.F., Baker, J., Jarvis, K.E., Mason, P., Menzies, M.A., 2000. On and off the North China Craton: where is the Archaean keel? J. Petrol. 41, 933–950.

Farquharson, C.G., Oldenburg, D.W., 2004. A comparison of automatic techniques for estimating the regularization parameter in non-linear inverse problems. Geophys. J. Int. 156, 411–425.

Fishwick, S., Heintz, M., Kennett, B., Reading, A.M., Yoshizawa, K., 2008. Steps in lithospheric thickness within eastern Australia, evidence from surface wave tomography. Tectonics 27, TC4009.

Fullea, J., Muller, M.R., Jones, A.G., 2011. Electrical conductivity of continental lithospheric mantle from integrated geophysical and petrological modeling: application to the Kaapvaal Craton and Rehoboth Terrane, southern Africa. J. Geophys. Res. 116, B10202.

Gao, S., Rudnick, R.L., Yuan, H., Liu, X., Liu, Y., Xu, W., Ling, W., Ayers, J., Wang, X., Wang, Q., 2004. Recycling lower continental crust in the North China craton. Nature 432, 892–897.

Gao, S., Rudnick, R.L., Xu, W., Yuan, H., Liu, Y., Walker, R.J., Puchtel, I.S., Liu, X., Huang, H., Wang, X., et al., 2008. Recycling deep cratonic lithosphere and generation of intraplate magmatism in the North China Craton. Earth Planet. Sci. Lett. 270, 41–53.

Glover, P.W.J., Hole, M.J., Pous, J., 2000. A modified Archie's law for two conducting phases. Earth Planet. Sci. Lett. 180, 369–383.

Griffin, W.L., Zhang, A.D., O'Reilly, S.Y., Ryan, C.G., 1998. Phanerozoic evolution of the lithosphere beneath the Sino-Korean craton. In: Flower, M.F.J., Chung, A.L., Lo, C.H., Lee, T.Y. (Eds.), Mantle Dynamics and Plate Interactions in East Asia, Geodynamics Series 27. AGU, Washington, DC, pp. 107–126.

Groom, R.W., Bailey, R.C., 1991. Analytic investigations of the effects of near-surface three-dimensional galvanic scatterers on MT tensor decompositions. Geophysics 56, 496–518.

Haak, V., Hutton, R., 1986. Electrical resistivity in continental lower crust. Geol. Soc., London, Spec. Publ. 24, 35–49.

Hirth, G., Evans, R.L., Chave, A.D., 2000. Comparison of continental and oceanic mantle electrical conductivity: is the Archean lithosphere dry? Geochem. Geophys. Geosyst. 1, 2000GC000048.

Hu, S.B., He, L.J., Wang, J.Y., 2000. Heat flow in the continental area of China: a new data set. Earth Planet. Sci. Lett. 179, 407–419.

Huang, Z.X., Li, H.Y., Zheng, Y.J., Peng, Y.J., 2009. The lithosphere of North China Craton from surface wave tomography. Earth Planet. Sci. Lett. 288, 164–173.

Jian, P., Liu, D.Y., Kröner, A., Windley, B.F., Shi, Y.R., Zhang, W., Zhang, F.Q., Miao, L.C., Zhang, L.Q., Tomurhuu, D., 2010. Evolution of a Permian intraoceanic arc–trench system in the Solonker suture zone, Central Asian Orogenic Belt, China and Mongolia. Lithos 118, 169–190.

Jones, A.G., 1988. Static shift of magnetotelluric data and its removal in a sedimentary basin environment. Geophysics 53, 967–978.

Jones, A.G., 2006. Electromagnetic interrogation of the anisotropic earth: looking into the earth with polarized spectacles. Phys. Earth Planet. Inter. 158, 281–291.

Jones, A.G., Craven, J.A., 2004. Area selection for diamond exploration using deep-probing electromagnetic surveying. Lithos 77, 765–782.

Jones, A.G., Katsube, T.J., Schwann, P., 1997. The longest conductivity anomaly in the world explained: sulphides in fold hinges causing very high electrical anisotropy. J. Geomagn. Geoelectr. 49, 1619–1629.

Jones, A.G., Ledo, J., Ferguson, I.J., 2005. Electromagnetic images of the Trans-Hudson orogen: the North American Central Plains anomaly revealed. Can. J. Earth Sci. 42, 457–478.

Jones, A.G., Evans, R.L., Eaton, D.W., 2009. Velocity–conductivity relationships for mantle mineral assemblages in Archean cratonic lithosphere based on a review of laboratory data and Hashin-Shtrikman extremal bounds. Lithos 109, 131–143.

Jones, A.G., Fullea, J., Evans, R.L., Muller, M.R., 2012. Water in cratonic lithosphere: calibrating laboratory-determined models of electrical conductivity of mantle minerals using geophysical and petrological observations. Geochem. Geophys. Geosyst. 13, Q06010.

Karato, S., 1990. The role of hydrogen in the electrical conductivity of the upper mantle. Nature 347, 272–273.

Karato, S., Wu, P., 1993. Rheology of the upper mantle: a synthesis. Science 260, 771–778.

Kennedy, C.S., Kennedy, G.C., 1976. The equilibrium boundary between graphite and diamond. J. Geophys. Res. 81, 2467–2470.

Kröner, A., Hegner, E., Lehmann, B., Heinhorst, J., Wingate, M.T.D., Liu, D.Y., Ermelov, P., 2008. Palaeozoic arc magmatism in the Central Asian Orogenic Belt of Kazakhstan: SHRIMP zircon ages and whole-rock Nd isotopic systematics. J. Asian Earth Sci. 32, 118–130.

Kusky, T.M., Windley, B.F., Zhai, M.G., 2007. Tectonic evolution of the North China Block: from orogen to craton to orogen. Geol. Soc., London, Spec. Publ. 280, 1–34.

Lebedev, S., Meier, T., van der Hilst, R.D., 2006. Asthenospheric flow and origin of volcanism in the Baikal Rift area. Earth Planet. Sci. Lett. 249, 415–424.

Ledo, J., 2006. 2-D versus 3-D magnetotelluric data interpretation. Surv. Geophys. 27, 511–543.

Ledo, J., Jones, A.G., 2005. Temperature of the upper mantle beneath the Intermontane Belt, northern Canadian Cordillera, determined from combining mineral composition, electrical conductivity laboratory studies and magnetotelluric field observations. Earth Planet. Sci. Lett. 236, 258–268.

Li, M.M., He, Y.M., 2011. Lithospheric structure beneath northeastern boundary region of the North China Craton from Rayleigh wave dispersion inversion. Acta Seismol. Sin. 33, 143–155 (in Chinese).

Li, J., Niu, F., 2010. Seismic anisotropy and mantle flow beneath northeast China inferred from regional seismic networks. J. Geophys. Res. 115, B12327.

Li, Y.Y., Yang, Y.S., 2011. Gravity data inversion for the lithospheric density structure beneath North China Craton from EGM 2008 model. Phys. Earth Planet. Inter. 189, 9–26.

Li, Z.A., Lee, C.A., Peslier, A.H., Lenardic, A., Mackwell, S.J., 2008. Water contents in mantle xenoliths from the Colorado Plateau and vicinity: implications for the mantle rheology and hydration-induced thinning of continental lithosphere. J. Geophys. Res. 113, B09210.

Li, W.H., Keller, G.R., Gao, R., Li, Q.S., Cox, C., Hou, H.S., Li, Y.K., Guan, Y., Zhang, S.H., 2013. Crustal structure of the northern margin of the North China Craton and adjacent region from SinoProbe02 North China seismic WAR/R experiment. Tectonophysics 606, 116–126.

Liu, D.Y., Nutman, A.P., Compston, W., Wu, J.S., Shen, Q.H., 1992. Remnants of ⩾3800 Ma crust in the Chinese part of the Sino-Korean Craton. Geology 20, 339–342.

Lizarralde, D., Chave, A., Hirth, G., Schultz, A., 1995. Northeastern Pacific mantle conductivity profile from long-period magnetotelluric sounding using Hawaii-to-California submarine cable data. J. Geophys. Res. 100, 17837–17854.

Lu, Z.X., Xia, H.K., 1993. Geoscience transect from Dong Ujimqin of Inner Mongolia to Donggou of Liaoning. Acta Geophys. Sin. 36, 765–772 (in Chinese).

Lu, Z.X., Xia, H.K., Zhao, G.M., Zhang, G.C., Dong, B.Z., Meng, B.Z., Li, P., 1993. Synthetic geophysics feature of geoscience transection from Dong Ujimqin Qi, Nei Mongol to Dong Gou, Liaoning. Seismol. Res. Northeast China 9, 1–12 (in Chinese).

McNeice, G.W., Jones, A.G., 2001. Multisite, multifrequency tensor decomposition of magnetotelluric data. Geophysics 66, 158–173.

Menzies, M.A., Fan, W.M., Zhang, M., 1993. Palaeozoic and Cenozoic lithoprobes and the loss of 120 km of Archean lithosphere, Sino-Korean craton, China. In: Prichard, H.M., Alabaster, T., Harris, N.B.W., Neary, C.R. (Eds.), Magmatic Processes and Plate Tectonics, vol. 76. Geological Society of London, Special Publications, pp. 71–81.

Miao, L., Zhang, F., Fan, W.M., Liu, D., 2007. Phanerozoic evolution of the Inner Mongolia-Daxinganling orogenic belt in North China: constraints from geochronology of ophiolites and associated formations. Geol. Soc., London, Spec. Publ. 280, 223–237.

Niu, Y.L., 2005. Generation and evolution of basaltic magmas: some basic concepts and a new view on the origin of Mesozoic–Cenozoic basaltic volcanism in eastern China. Geol. J. China Univ. 11, 9–46.

Niu, X., Lu, Z.X., Jiang, D.L., Lei, Q.Q., Shi, S.C., 2000. Crust-mantle structure feature and the seismic activity of the main tectonic units in the North Tanlu fault zone. Acta Seismol. Sin. 13, 159–165.

O'Neill, C.J., Lenardic, A., Griffin, W.L., O'Reilly, S.Y., 2008. Dynamics of cratons in an evolving mantle. Lithos 102, 12–24.

Parker, R.L., Booker, J.R., 1996. Optimal one-dimensional inversion and bounding of magnetotelluric apparent resistivity and phase measurements. Phys. Earth Planet. Inter. 98, 269–282.

Peslier, A.H., Woodland, A.B., Bell, D.R., Lazarov, M., 2010. Olivine water contents in the continental lithosphere and the longevity of cratons. Nature 467, 78–81.

Pommier, A., 2014. Interpretation of magnetotelluric results using laboratory measurements. Surv. Geophys. 35, 41–84.

Rao, C.K., Jones, A.G., Moorkamp, M., 2007. The geometry of the Iapetus Suture Zone in central Ireland deduced from a magnetotelluric study. Phys. Earth Planet. Inter. 161, 134–141.

Rippe, D., Unsworth, M.J., Currie, C.A., 2013. Magnetotelluric constraints on the fluid content in the upper mantle beneath the southern Canadian Cordillera: implications for rheology. J. Geophys. Res. 118, 5601–5624.

Rodi, W., Mackie, R.L., 2001. Nonlinear conjugate gradient algorithm for 2-D magnetotelluric inversion. Geophysics 66, 174–178.

Selway, K., 2014. On the causes of electrical conductivity anomalies in tectonically stable lithosphere. Surv. Geophys. 35, 219–257.

Selway, K., Yi, J., Karato, S.I., 2014. Water content of the Tanzanian lithosphere from magnetotelluric data: implications for cratonic growth and stability. Earth Planet. Sci. Lett. 338, 175–186.

Shomail, Z.H., Roberts, R.G., Pedersen, L.B., the TOR Working Group, 2006. Lithospheric structure of the Tornquist Zone resolved by nonlinear P and S teleseismic tomography along the TOR array. Tectonophysics 416, 133–149.

Spratt, J.E., Jones, A.G., Jackson, V.A., Collins, L., Avdeeva, A., 2009. Lithospheric geometry of the Wopmay orogen from a Slave craton to Bear Province magnetotelluric transect. J. Geophys. Res. 114, B01101.

Sun, Y.J., Dong, S.W., Zhang, H., Li, H., Shi, Y.L., 2013. 3D thermal structure of the continental lithosphere beneath China and adjacent regions. J. Asian Earth Sci. 62, 697–704.

Tang, Q.S., Chen, L., 2008. Structure of the crust and uppermost mantle of the Yanshan Belt and adjacent regions at the northeastern boundary of the North China Craton from Rayleigh wave dispersion analysis. Tectonophysics 455, 43–52.

Tauber, S., Banks, R., Ritter, O., Weckmann, U., 2003. A high-resolution magnetotelluric survey of the Iapetus Suture Zone in southwest Scotland. Geophys. J. Int. 153, 548–568.

Unsworth, M., Wei, W.B., Jones, A.G., Li, S.H., Bedrosian, P., Booker, J., Jin, S., Deng, M., Tan, H.D., 2004. Crustal and upper mantle structure of northern Tibet imaged with magnetotelluric data. J. Geophys. Res. 109, B02403. http://dx.doi.org/10.1029/2002JB002305.

Varentsov, I.M., Sokolova, E.Y., BEAR, W.G., 2003. Diagnostics and suppression of auroral distortions in the transfer operators of the EM field in the BEAR experiment, Izvestya. Phys. Solid Earth 39, 283–307.

Wang, Y., Cheng, S.H., 2012. Lithospheric thermal structure and rheology of the eastern China. J. Asian Earth Sci. 47, 51–63.

Wang, D.J., Mookherjee, M., Xu, Y.S., Karato, S., 2006. The effect of water on the electrical conductivity of olivine. Nature 443, 977–980.

Wang, Q., Bagdassarov, N., Xia, Q.K., Zhu, B.B., 2014. Water contents and electrical conductivity of peridotite xenoliths from the North China Craton: implication for water distribution in the upper mantle. Lithos 189, 105–126.

Wannamaker, P.E., Hohmann, G.W., Ward, S.H., 1984. Magnetotelluric responses of three-dimensional bodies in layered earths. Geophysics 49, 1517–1533.

Wei, Z.G., Chen, L., Yang, X.L., 2011. Transverse variations of crustal thickness and (V_p/V_s) ratio under the stations in the Liaodong anticline Yanshan belt Xingmeng orogenic belt and their tectonic implications. Chin. J. Geophys. 11, 2799–2808.

Windley, B.F., Alexeiev, D., Xiao, W.J., Kröner, A., Badarch, G., 2007. Tectonic models for accretion of the Central Asian Orogenic Belt. J. Geol. Soc. 164, 31–47.

Wu, F.Y., Walker, R.J., Ren, X.W., Sun, D.Y., Zhou, X.H., 2003. Osmium isotopic constraints on the age of lithospheric mantle beneath Northeastern China. Chem. Geol. 196, 107–129.

Wu, F.Y., Lin, J.Q., Wilde, S.A., Zhang, X.O., Yang, J.H., 2005. Nature and significance of the Early Cretaceous giant igneous event in eastern China. Earth Planet. Sci. Lett. 233, 103–119.

Wu, F.Y., Walker, R.J., Yang, Y.H., Yuan, H.L., Yang, J.H., 2006. The chemical–temporal evolution of lithospheric mantle underlying the North China Craton. Geochim. Cosmochim. Acta 70, 5013–5034.

Xia, Q.K., Hao, Y.T., Li, P., Deloule, E., Coltorti, M., Dallai, L., Yang, X.Z., Feng, M., 2010. Low water content of the Cenozoic lithospheric mantle beneath the eastern part of the North China Craton. J. Geophys. Res. 115, B07207.

Xia, Q.K., Liu, J., Liu, S.C., Kovács, I., Feng, M., Dang, L., 2013. High water content in Mesozoic primitive basalts of the North China Craton and implications on the destruction of cratonic mantle lithosphere. Earth Planet. Sci. Lett. 361, 85–97.

Xiao, W.J., Windley, B.F., Hao, J., Zhai, M.G., 2003. Accretion leading to collision and the Permian Solonker suture, Inner Mongolia, China: termination of the central Asian orogenic belt. Tectonics 22, 1609. http://dx.doi.org/10.1029/2002TC001484.

Xu, Y.G., 2001. Thermo-tectonic destruction of the Archaean lithospheric keel beneath the Sino-Korean Craton in China: evidence, timing and mechanism. Phys. Chem. Earth 26, 747–757.

Xu, Y.G., 2007. Diachronous lithospheric thinning of the North China Craton and formation of the Daxin'anling-Taihangshan gravity lineament. Lithos 96, 281–298.

Xu, J.W., Zhu, G., 1994. Tectonic models of the Tan-Lu fault zone, eastern China. Int. Geol. Rev. 36, 771–784.

Xu, J.W., Zhu, G., Tong, W.X., Cui, K.R., Liu, Q., 1987. Formation and evolution of the Tancheng-Lujiang wrench fault system: a major shear system to the northwest of the Pacific Ocean. Tectonophysics 134, 273–310.

Xu, Y.G., Huang, X.L., Ma, J.L., Wang, Y.B., Iizuka, Y., Xu, J.F., Wang, Q., Wu, X.Y., 2004. Crust-mantle interaction during the tectono-thermal reactivation of the North China Craton: constraints from SHRIMP zircon U–Pb chronology and geochemistry of Mesozoic plutons from western Shandong. Contrib. Miner. Petrol. 147, 750–767.

Xu, Y.G., Li, H.Y., Pang, C.J., He, B., 2009. On the timing and duration of the destruction of the North China Craton. Chin. Sci. Bull. 54, 3379–3396.

Xu, W.W., Zheng, T.Y., Zhao, L., 2011. Mantle dynamics of the reactivating North China Craton: constraints from the topographies of the 410-km and 660-km discontinuities. Sci. China Earth Sci. 54 (6), 881–887.

Yang, X.Z., Xia, Q.K., Deloule, E., Dallai, L., Fan, Q., Feng, M., 2008. Water in minerals of the continental lithospheric mantle and overlying lower crust: a comparative study of peridotite and granulite xenoliths from the North China Craton. Chem. Geol. 256, 33–45.

Yang, W., Teng, F.Z., Zhang, H.F., Li, S.G., 2012. Magnesium isotopic systematics of continental basalts from the North China craton: implications for tracing subducted carbonate in the mantle. Chem. Geol. 328, 185–194.

Yoshino, T., Noritake, F., 2011. Unstable graphite films on grain boundaries in crustal rocks. Earth Planet. Sci. Lett. 306, 186–192.

Yoshino, T., Matsuzaki, T., Shatskiy, A., Katsura, T., 2009. The effect of water on the electrical conductivity of olivine aggregates and its implications for the electrical structure of the upper mantle. Earth Planet. Sci. Lett. 288, 291–300.

Yoshino, T., Matsuzaki, T., Shatskiy, A., Katsura, T., 2014. Corrigendum to "The effect of water on the electrical conductivity of olivine aggregates and its implications for the electrical structure of the upper mantle" [Earth and Planetary Science Letters 288 (2009), 291–300.]. Earth Planet. Sci. Lett. 391, 135–136.

Zeng, Q.D., Liu, J.M., Zhang, Z.L., Chen, W.J., Zhang, W.Q., 2011. Geology and geochronology of the Xilamulun molybdenum metallogenic belt in eastern Inner Mongolia, China. Int. J. Earth Sci. 100, 1791–1809.

Zhang, H.F., 2009. Peridotite-melt interaction: a key point for the destruction of cratonic lithospheric mantle. Chin. Sci. Bull. 54, 3417–3437.

Zhang, L., Liu, J.S., Hao, T.Y., Liu, J.H., Xu, Y., 2007. Seismic tomography of the crust and upper mantle in the Bohai Bay Basin and its adjacent regions. Sci. China, Ser. D: Earth Sci. 50, 1810–1822.

Zhang, H.F., Goldstein, S.L., Zhou, X.H., Sun, M., Zheng, J.P., Cai, Y., 2008. Evolution of subcontinental lithospheric mantle beneath eastern China: Re–Os isotopic evidence from mantle xenoliths in Paleozoic kimberlites and Mesozoic basalts. Contrib. Miner. Petrol. 155, 271–293.

Zhang, L.C., Wu, H.Y., Wan, B., Chen, Z.G., 2009. Ages and geodynamic settings of Xilamulun Mo–Cu metallogenic belt in the northern part of the North China Craton. Gondwana Res. 16, 243–254.

Zhao, L., Zheng, T.Y., 2007. Complex upper-mantle deformation beneath the North China Craton: implications for lithospheric thinning. Geophys. J. Int. 170, 1095–1099.

Zhao, G.C., Wilde, S.A., Cawood, P.A., Sun, M., 2001. Archean blocks and their boundaries in the North China Craton: lithological, geochemical, structural and P–T path constraints and tectonic evolution. Precambr. Res. 107, 45–73.

Zhao, G.C., Sun, M., Wilde, S.A., Li, S.Z., 2003. Assembly, accretion and breakup of the Paleo-Mesoproterozoic Columbia Supercontinent: records in the North China Craton. Gondwana Res. 6, 417–434.

Zhao, G.C., Sun, M., Wilde, S.A., Li, S.Z., 2005. Late Archean to Paleoproterozoic evolution of the North China Craton: key issues revisited. Precambr. Res. 136, 177–202.

Zhao, L.F., Xie, X.B., Wang, W.M., Zhang, J.H., Yao, Z.X., 2010. Seismic Lg-wave Q tomography in and around Northeast China. J. Geophys. Res. 115, B08307.

Zhao, L., Allen, R.M., Zheng, T., Zhu, R., 2012. High-resolution body-wave tomography models of the upper mantle beneath eastern China and the adjacent areas. Geochem. Geophys. Geosyst. 13, Q06007. http://dx.doi.org/10.1029/2012GC004119.

Zheng, J.P., O'Reilly, S.Y., Griffin, W.L., Lu, F.X., Zhang, M., 1998. Nature and evolution of Cenozoic lithospheric mantle beneath Shandong peninsula, Sino-Korean craton, eastern China. Int. Geol. Rev. 40, 471–499.

Zheng, J.P., Griffin, W.L., O Reilly, S.Y., Yu, C.M., Zhang, H.F., Pearson, N., Zhang, M., 2007a. Mechanism and timing of lithospheric modification and replacement beneath the eastern North China Craton: peridotitic xenoliths from the 100 Ma Fuxin basalts and a regional synthesis. Geochim. Cosmochim. Acta 71, 5203–5225.

Zheng, T., Chen, L., Zhao, L., Zhu, R., 2007b. Crustal structure across the Yanshan belt at the northern margin of the North China Craton. Phys. Earth Planet. Inter. 161, 36–49.

Zheng, T.Y., Zhao, L., Xu, W.W., Zhu, R.X., 2008. Insight into modification of North China Craton from seismological study in the Shandong Province. Geophys. Res. Lett. 35, L22305.

Zheng, T.Y., Zhu, R.X., Zhao, L., Ai, Y.S., 2012. Intralithospheric mantle structures recorded continental subduction. J. Geophys. Res. 117, B03308.

Zhou, X.H., Sun, M., Zhang, G.H., Chen, S.H., 2002. Continental crust and lithospheric mantle interaction beneath North China: isotopic evidence from granulite xenoliths in Hannuoba, Sino-Korean craton. Lithos 62, 111–124.

Zhu, R., Zheng, T.Y., 2009. Destruction geodynamics of the North China Craton and its Paleoproterozoic plate tectonics. Chin. Sci. Bull. 54, 3354–3366.